

Response to editor comments (our replies in bold)

Dear Kate E. Ashley et al.,

Thank you for submitting your revised version of your manuscript "Mid-Holocene Antarctic sea-ice increase driven by marine ice sheet retreat". Overall, I think you have done a very good job addressing the reviewer's comments. Before accepting the paper, I have a few minor comments that I would like you to address.

L56: In your responses to the reviewer 1 you stated that you would change from Antarctica to East Antarctica. I cannot see that this have been done.

We have corrected this (line 55).

L600: Please specify to where in the supplementary material you refer the reader.

We had added reference to Supplementary section S2.2 and Fig. S4 (line 535).

L609: Here you refer to IRD, but with no reference to any of the figures or to literature. Please add appropriate reference. In you results section you mention IRD, but purely with a reference to a published paper and with no reference to any figures where the data is shown. So, is IRD part of your results or not?

In lines 489-491 we state that there is a lack of IRD in unit 1 (Escutia et al., 2011), which is the focus of this paper. Thus, there is no data to show but we have added in a reference to Escutia et al., 2011 (lines 544-545).

L688: Instead of referring to "this study", refer to the figure showing the relevant data. Specify what type of proxies the other studies you use to support this statement is based on.

We have removed 'this study' and refer specifically to our HBI data (Fig. 4c); sea ice diatoms in core MD03-2601 (Crosta et al., 2008); methanesulfonic acid concentration in Taylor dome ice core (Steig et al., 1998); and sea ice diatoms in core JPC24 (Denis et al., 2010. See lines 621-624.

L765: Delete the first "patterns"?

We have edited this as suggested (line 704)

L735: In your response to reviewer 2 you stated that you would be more specific and instead of "most models" refer to "TRACE21". This has not been done. Furthermore, why not include Figure S6 in the manuscript instead of as a supplement as long as it is discussed here?

It is true that we originally suggested we would change that, however, we realised that as well as TRACE21, we also refer to the study by Lui et al., 2013 which analyses three coupled ocean-atmosphere models (CCSM3, FAMOUS and LOVECLIM), thus we are not only referring to the TraCE-21k simulation. We have now included Fig S6 in the main manuscript (Fig. 7)

Many of your figures are build-up of several panels/sub-figures (a, b, c,...). Occasionally you refer to the individual panels, but mostly you refer to the full figures without further specifications. Please check that whenever you only refer to one or a few of the datasets in a figure, specific with panels you refer to.

We have been through the manuscript and referred to the individual panels within figures where required.

Best regards,
Björg Risebrobakken
Editor Climate of the Past

1 **FRONT MATTER**

2 **Title**

3 Mid-Holocene Antarctic sea-ice increase driven by marine ice sheet retreat

4 **Authors**

5 Kate E. Ashley¹, -Robert McKay², Johan Etourneau³, Francisco J. Jimenez-Espejo^{3,4}, Alan Condron⁵,
6 Anna Albot², Xavier Crosta⁶, Christina Riesselman^{7,8}, Osamu Seki⁹, Guillaume Massé¹⁰, Nicholas R.
7 Gолledge^{2,11}, Edward Gasson¹², Daniel P. Lowry², Nicholas E. Barrand¹, Katelyn Johnson², Nancy
8 Bertler², Carlota Escutia³, Robert Dunbar¹³ and James A. Bendle^{1*}.

9 **Affiliations**

10 ¹School of Geography, Earth and Environmental Sciences, University of Birmingham, Edgbaston,
11 Birmingham, B15 2TT, UK

12 ²Antarctic Research Centre, Victoria University of Wellington, Wellington 6140, New Zealand

13 ³Instituto Andaluz de Ciencias de la Tierra (CSIC), Avenida de las Palmeras 4, 18100 Armilla, Granada,
14 Spain

15 ⁴Department of Biogeochemistry, Japan Agency for Marine-Earth Science and Technology
16 (JAMSTEC), Yokosuka 237-0061, Japan

17 ⁵Department of Geology and Geophysics, Woods Hole Oceanographic Institution, Woods Hole, MA
18 02543, USA

19 ⁶UMR-CNRS 5805 EPOC, Université de Bordeaux, 33615 Pessac, France

20 ⁷Department of Geology, University of Otago, Dunedin 9016, New Zealand

21 ⁸Department of Marine Science, University of Otago, Dunedin 9016, New Zealand

22 ⁹Institute of Low Temperature Science, Hokkaido University, Sapporo, Hokkaido, Japan

23 ¹⁰TAKUVIK, UMI 3376 UL/CNRS, Université Laval, 1045 avenue de la Médecine, Quebec City,
24 Quebec, Canada G1V 0A6

25 ¹¹GNS Science, Avalon, Lower Hutt 5011, New Zealand

26 ¹²Department of Geography, University of Sheffield, Winter Street, Sheffield, S10 2TN, UK

27 ¹³Department of Environmental Earth Systems Science, Stanford University, Stanford, CA 94305-2115

28

29 ***Corresponding Author:** email: j.bendle@bham.ac.uk

30

31 **1. ABSTRACT**

32 Over recent decades Antarctic sea-ice extent has increased, alongside widespread ice shelf thinning and
33 freshening of waters along the Antarctic margin. In contrast, Earth system models generally simulate a
34 decrease in sea ice. Circulation of water masses beneath large cavity ice shelves is not included in current
35 Earth System models and may be a driver of this phenomena. We examine a Holocene sediment core off
36 East Antarctica that records the Neoglacial transition, the last major baseline shift of Antarctic sea-ice,
37 and part of a late-Holocene global cooling trend. We provide a multi-proxy record of Holocene glacial
38 meltwater input, sediment transport and sea-ice variability. Our record, supported by high-resolution
39 ocean modelling, shows that a rapid Antarctic sea-ice increase during the mid Holocene (~4.5 ka) occurred
40 against a backdrop of increasing glacial meltwater input and gradual climate warming. We suggest that
41 mid-Holocene ice shelf cavity expansion led to cooling of surface waters and sea-ice growth which slowed
42 basal ice shelf melting. Incorporating this feedback mechanism into global climate models will be
43 important for future projections of Antarctic changes.

44

45 **2. INTRODUCTION**

46 Ice shelves and sea ice are intrinsically linked and represent fundamental components of the global
47 climate system, impacting ice-sheet dynamics, large-scale ocean circulation, and the Southern Ocean
48 biosphere. Antarctic ice-shelves with large sub-shelf cavities (e.g. Ross, Filchner-Ronne) play a key role
49 in regional sea-ice variations, by cooling and freshening surface ocean waters for hundreds of kilometres
50 beyond the ice shelf edge (Hellmer, 2004; Hughes *et al.*, 2014). Antarctic sea ice has expanded over the
51 past few decades, particularly in the western Ross Sea region (Turner *et al.*, 2016), alongside widespread
52 thinning of ice shelves (Paolo *et al.*, 2015) and freshening along the Antarctic margin (Jacobs *et al.*,
53 2002; Aoki *et al.*, 2013). The drivers and feedbacks involved in these decadal trends are still poorly
54 understood, hampered by the sparse and short-term nature of meteorological, oceanographic and
55 glaciological observations (Jones *et al.*, 2016), and thus establishing the long-term trajectory for [East](#)
56 Antarctic sea ice on the background of accelerated ice sheet loss remains a challenge. Marine sediment
57 cores provide a longer-term perspective and highlight a major baseline shift in coastal sea ice ~4.5 ka
58 ago (Steig *et al.*, 1998; Crosta *et al.*, 2008; Denis *et al.*, 2010) which characterizes the mid-Holocene
59 ‘Neoglacial’ transition in the Antarctic. A mechanistic driver for this climate shift currently remains

60 unresolved, but we propose that two interrelated aspects of the last deglaciation are significantly
61 underrepresented in current models of this transition: (i) the retreat of grounded ice sheets from the
62 continental shelves of Antarctica, and (ii) the subsequent development of large ice shelf cavities during
63 the Holocene. Both factors would significantly alter water mass formation on Antarctica's continental
64 shelves, which today are major source regions of Antarctic Bottom Water (AABW) and Antarctic
65 Surface Water (AASW). These interrelated processes are underrepresented in coupled ocean-atmosphere
66 models which currently do not simulate the timing, magnitude and rapid onset of the Neoglacial
67 (Supplementary Materials).

68
69 Integrated Ocean Drilling Program (IODP) Expedition 318 cored a 171 m thick deposit of laminated
70 diatomaceous ooze at Site U1357 offshore Adélie Land (Fig. 1), deposited over the past 11,400 years.
71 Here, we present a new Holocene record of glacial meltwater, sedimentary input and local sea ice
72 concentrations from Site U1357 using compound-specific hydrogen isotopes of fatty acid biomarkers
73 ($\delta^2\text{H}_{\text{FA}}$), terrigenous grain size (mud percent, sorting), natural gamma radiation, biogenic silica
74 accumulation, highly-branched isoprenoid alkenes (HBIs) and Ba/Ti ratios (Fig. 4 and 5).

75
76 We interpret $\delta^2\text{H}_{\text{FA}}$ (Fig. 24a) fluctuations in Adélie Drift sediments as a record of meltwater input from
77 isotopically-depleted glacial ice. Antarctic glacial ice is highly depleted in ^2H compared to ocean
78 water, thus creating highly contrasting end-member values for the two major H source pools. Grain size,
79 natural gamma radiation (NGR) and terrigenous and biosiliceous mass accumulation rates (MARs)
80 reflect changing sediment delivery either driven via local glacial meltwater discharge or advection of
81 suspended sediment by oceanic currents. The diene/triene HBI ratio is used as a proxy for coastal sea ice
82 presence (Massé *et al.*, 2011). Ba/Ti enrichment is considered to reflect enhanced primary productivity.
83 These records allow a unique opportunity to reconstruct the magnitude of the coupled response of the
84 ocean and ice sheet during the Neoglacial transition. Details on all proxies and associated uncertainties
85 can be found in Section S2 of the Supplementary Information.

86 87 88 **3. MATERIALS AND METHODS**

89 90 **3.1 Organic geochemical analyses**

91 **3.1.1 Fatty acid extraction**

92 Lipid extraction of sediment samples was performed at the Royal Netherlands Institute for Sea Research
93 (NIOZ). Freeze-dried and homogenized samples were extracted by Dionex™ accelerated solvent
94 extraction (DIONEX ASE 200) using a mixture of dichloromethane (DCM)/methanol (MeOH) (9:1,
95 v/v) at a temperature of 100°C and a pressure of 7.6×10^6 Pa (Kim *et al.*, 2010).

96
97 Compound separation was undertaken at University of Glasgow, UK. The total lipid extract was
98 separated over an aminopropyl silica gel column and the total acid fraction was eluted into an 8ml vial
99 with 4% acetic acid in ethyl-ether solution (Huang *et al.*, 1999). Derivatisation to Fatty Acid Methyl
100 Esters was achieved by adding 200 µl of MeOH containing 14% v/v Boron trifluoride to the 8ml vial
101 containing the TAF. FAMES were recovered and cleaned up by eluting through a pre-cleaned 3cm silica
102 gel column (60 Å; 35-70) with 4ml of hexane and 4ml of DCM (containing the FAMES). $\delta^2\text{H}$ values
103 indicate depletion against the international standards: Vienna Pee Dee Belemnite (V-PDB) is the
104 standard for $\delta^{13}\text{C}$ and Vienna Standard Mean Ocean Water (V-SMOW) for $\delta^2\text{H}$.

105
106 3.1.2 Fatty acid hydrogen isotope analysis Compound specific hydrogen isotope analyses of FAMES was
107 performed at the Institute of Low Temperature Science, Hokkaido University. $\delta^2\text{H}$ values were obtained
108 using a CS-IRMS system with a HP 6890 gas chromatograph and a ThermoQuest Finnigan MAT Delta
109 Plus XL mass spectrometer. Separation of the FAMES was achieved with a HP-5 MS fused silica
110 capillary column (30 m x 0.32 mm i.d., film thickness of 0.25 µm) with a cooled on-column injector. An
111 *n*-alkane and a reference gas whose isotopic values were known was co-injected with the samples as an
112 internal isotopic standard for $\delta^2\text{H}$. A laboratory standard (Mix F8 of FAMES from Indiana University)
113 containing C_{10} – C_{30} FAMES was analyzed daily to check the accuracy and the drift of the instrument and
114 to normalize the data to the SMOW/SLAP isotopic scale. The H^{3+} factor was measured every three days.

115
116 **3.1.3 HBIs**

117 Highly branched isoprenoids (HBI) alkenes were extracted at Laboratoire d'Océanographie et du
118 Climat: Experimentations et Approches Numériques (LOCEAN), separately from the fatty acids, using a
119 mixture of 9mL $\text{CH}_2\text{Cl}_2/\text{MeOH}$ (2:1, v:v) to which 7 hexyl nonadecane (*m/z* 266) was added as an
120 internal standard, following the Belt *et al* (2007) and Massé *et al.* (2011) protocols. Several sonication
121 and centrifugation steps were applied in order to properly extract the selected compounds (Etourneau *et*

122 *al.*, 2013). After drying with N₂ at 35°C, the total lipid extract was fractionated over a silica column into
123 an apolar and a polar fraction using 3 mL hexane and 6 mL CH₂Cl₂/MeOH (1:1, v:v), respectively. HBIs
124 were obtained from the apolar fraction by the fractionation over a silica column using hexane as eluent
125 following the procedures reported by Belt *et al.* (2007; Massé *et al.*, 2011). After removing the solvent
126 with N₂ at 35°C, elemental sulfur was removed using the TBA (Tetrabutylammonium) sulfite method
127 (Jensen *et al.*, 1977; Riis and Babel, 1999). The obtained hydrocarbon fraction was analyzed within an
128 Agilent 7890A gas chromatograph (GC) fitted with 30 m fused silica Agilent J&C GC column (0.25 mm
129 i.d., 0.25 µm film thickness), coupled to an Agilent 5975C Series mass selective detector (MSD).
130 Spectra were collected using the Agilent MS-Chemstation software. Individual HBIs were identified on
131 the basis of comparison between their GC retention times and mass spectra with those of previously
132 authenticated HBIs (Johns *et al.*, 1999) using the Mass Hunter software. Values are expressed as
133 concentration relative to the internal standard.

134

135 **3.2 Inorganic geochemical analysis and electronic microscopy**

136 Major element concentrations were obtained using X-Ray Fluorescence Scanner on 412 analyses
137 measured directly over undisturbed sediment sections. The bulk major element composition included in
138 this study was measured between sections U1357B-1H-2 to U1357-19H-5 continuously each 50 cm. We
139 used an Avaatech X-ray fluorescence (XRF-Scanner) core scanner at the IODP-Core Repository/Texas
140 A&M University laboratories (USA) during December 2010. Non-destructive XRF core-scanning
141 measurements were performed over 1 cm² area with slit size of 10 mm, a current of 0.8 mA and
142 sampling time of 45 seconds at 10 kV in order to measure the relative content of titanium (Ti) and
143 barium (Ba).

144

145 Field emission scanning electron microscopy (FESEM) images and corresponding spectrum were
146 obtained with an AURIGA FIB-FESEM Carl Zeiss SMT at Centro de Instrumentación Científica,
147 Granada University, Spain

148

149 **3.3 Grain size analyses**

150 A total of 341 samples were prepared for grain size analysis. Samples were treated for removal of
151 biogenic opal with a 1M sodium hydroxide NaOH solution and incubated in a water bath at 80°C for 24
152 hours. This procedure was repeated twice due to an incomplete dissolution of diatoms observed in smear

153 slides. The samples were then treated with H₂O₂ to remove organic material at 80°C for 24 hours.
154 Samples were measured using a Beckman Coulter LS 13 320 Laser Diffraction Particle Size Analyser
155 (LPSA). Prior to grain size analysis, ~30 mL of 0.5 g/L Calgon (sodium hexametaphosphate) was added
156 to the samples, and sonicated and stirred in order to disperse the grains and prevent clumping.

157

158 **3.4 Biogenic silica**

159 Biogenic silica concentrations (wt% BSi) were measured on 349 discrete samples using a molybdate
160 blue spectrophotometric method modified from (Strickland and Parsons, 1970; DeMaster, 1981).
161 Analytical runs included replicates from the previous sample group and from within the run, and each
162 run was controlled by 10 standards and a blank with dissolved silica concentrations ranging from 0 µM
163 to 1200 µM. For each analysis, ~7 mg of dry, homogenized sediment was leached in 0.1M NaOH at
164 85°C, and sequential aliquots were collected after 2, 3, and 4 hours. Following addition of reagents,
165 absorbance of the 812 nm wavelength was measured using a Shimadzu UV-1800 spectrophotometer.
166 Dissolved silica concentration of each unknown was calculated using the standard curve, and data from
167 the three sampling hours were regressed following the method of DeMaster (1981) to calculate wt%
168 BSi. In our U1357B samples, wt% BSi ranges from maximum of ~60% in early and mid-Holocene light
169 laminae to a minimum of 31% in late Holocene dark laminae. The average standard deviation of
170 replicate measurements is 0.5%.

171

172 **3.5 Model simulations**

173 All numerical calculations were performed using the Massachusetts Institute of Technology general
174 circulation model (MITgcm) (Marshall *et al.*, 1997); a three-dimensional, ocean sea-ice, hydrostatic,
175 primitive equation model. The experiments presented here were integrated on a global domain projected
176 onto a cube-sphere grid to permit a relatively even grid spacing and to avoid polar singularities (Adcroft
177 *et al.*, 2004; Condon and Winsor, 2012). The ocean grid has a mean, eddy-permitting, horizontal grid
178 spacing of 1/6° (18-km) with 50 vertical levels ranging in thickness from 10m near the surface to
179 approximately 450m at the maximum model depth. The ocean model is coupled to a sea-ice model in
180 which ice motion is driven by forces generated by the wind, ocean, Coriolis force, and surface elevation
181 of the ocean, while internal ice stresses are calculated using a viscous-plastic (VP) rheology, as
182 described in Zhang and Hibler (1997). In all experiments, the numerical model is configured to simulate
183 present-day (modern) conditions: Atmospheric forcings (wind, radiation, rain, humidity etc.) are

184 prescribed using 6-hourly climatological (1979-2000) data from the ERA-40 reanalysis product
185 produced by the European Centre for Medium-range Weather Forecasts and background rates of runoff
186 from the ice sheet to the ocean are based on the numerical ice sheet model of Pollard and Deconto
187 (2016) integrated over the same period (1979-2000). To study the pathway of meltwater in the ocean,
188 additional fresh (i.e. 0 psu) water was released into the surface layer of the ocean model at the grid
189 points closest to the front of the Ross Ice Shelf. Five different discharge experiments were performed by
190 releasing meltwater into this region at rates of 0.01 Sv ($Sv = 10^6 \text{ m}^3/\text{s}$), 0.05 Sv, 0.1 Sv, 0.5 Sv, and 1 Sv
191 for the entire duration of each experiment (~3.5 years).

192

193 **4. ENVIRONMENTAL SETTING AND INTERPRETATION OF PROXY DATA**

194 We utilize a 180 m thick sediment core that was recovered from the Wilkes Land Margin continental
195 shelf in the Adélie Basin (IODP Site U1357). This core targeted an expanded sediment drift (Adélie
196 Drift) and provides a high-resolution Holocene record of climate variability. Below we provide pertinent
197 details on this unique site and on our application of compound specific $\delta^2\text{H}$ measurements on algal
198 biomarkers as a novel meltwater proxy. Further details on proxy interpretation (Ba/Ti, grain size, HBIs)
199 are given in the Supplementary Materials.

200

201 **4.1 The Adélie Drift**

202 Site U1357 is located in the Dumont d'Urville Trough of the Adélie Basin, ca. 35 km offshore from
203 Adélie Land (66°24.7990'S, 140°25.5705'E; Fig 1). This is a >1000 m deep, glacially scoured
204 depression on the East Antarctic continental shelf, bounded to the east by the Adélie Bank. Further east
205 lays the Adélie Depression and the Mertz Bank, the latter located north of the Mertz Glacier floating ice
206 tongue. The Adélie Land region is dissected by several glaciers which could potentially contribute
207 terrigenous sediment into the coastal zone with the core site located 40 km to the north of the Astrolabe
208 Glacier, and ca. 75 and 300 km northwest of the Zélée and Mertz glaciers, respectively.

209

210 The site itself is located within the Dumont d'Urville polynya (DDUP), which has a summer (winter)
211 extent of 13,020 km² (920 km²), but is also directly downwind and downcurrent of the much larger and
212 highly productive Mertz Glacier polynya (MGP) to the east, with a summer (winter) extent of 26,600
213 km² (591 km²) (Arrigo and van Dijken, 2003). The MGP forms as a result of reduced sea-ice westward
214 advection due to the presence of the Mertz Glacier Tongue (Massom *et al.*, 2001) and strong katabatic

215 winds which blow off the Antarctic ice sheet with temperatures below -30°C (Bindoff *et al.*, 2000).
216 Katabatic winds freeze the surface waters and blow newly formed ice away from the coast, making the
217 polynya an efficient sea-ice ‘factory’, with higher rates of sea-ice formation in comparison to non-
218 polynya ocean areas which undergo seasonal sea ice formation (Kusahara *et al.*, 2010). The MGP
219 produces 1.3% of the total Southern Ocean sea ice volume despite occupying less than 0.1% of total
220 Antarctic sea ice extent (Marsland *et al.*, 2004).

221
222 As a result of the upwelling polynya environments, the area along the Adélie Coast is characterized by
223 extremely high primary productivity, with the water column known to host significant amounts of
224 phytoplankton, dominated by diatoms (Beans *et al.*, 2008). The Mertz Glacier zone is generally
225 characterized by stratified waters in the summer, due to seasonal ice melt, with these conditions
226 corresponding to the highest phytoplankton biomass. The lack of ice cover means polynyas are the first
227 polar marine systems exposed to spring solar radiation, making them regions of enhanced biological
228 productivity compared to adjacent waters. A considerable amount of resultant sedimentation is focused
229 via the westward flowing currents from both of these polynyas within the deep, protected Adélie Basin,
230 resulting in a remarkably high sedimentation rate of ca. $1.5\text{-}2\text{ cm year}^{-1}$ at Site U1357 (Escutia *et al.*,
231 2011).

232
233 Although biogenic and terrigenous sediment is interpreted to be sourced locally in the Adélie Land
234 region, the mass accumulation rate of these sediments in this drift is associated with the intensity of
235 westward flowing currents (S2.2). Critically, these westward currents also act to transport water masses
236 from further afield, and Site U1357 is directly oceanographically downstream of the Ross Sea, meaning
237 the continental shelf in this region receives significant Antarctic Surface Water (ASSW) transported by
238 the Antarctic Slope Current (ASC) and Antarctic Coastal Current -from the Ross Sea embayment . Thus,
239 changes in the surface waters of the Ross Sea influence Site U1357. Whitworth *et al.* (1998) confirm the
240 continuity of the westward flowing ASC between the Ross Sea and the Wilkes Land margin. This flow
241 is largely associated with the Antarctic Slope Front, which reflects the strong density contrast between
242 AASW and Circumpolar Deep Water (CDW). McCartney and Donohue (2007) estimate that the
243 transport in the westward ASC, which links the Ross Sea to the Wilkes Land margin, reaches 76 Sv (Sv
244 = $10^6\text{ m}^3\text{ s}^{-1}$). However, Peña-Molino *et al.* (2016) measured a highly variable ASC flow at 113°E
245 ranging from 0 to 100 Sv with a mean of 21.2 Sv. This contributes to a cyclonic gyre, which together

246 with the ASC dominate the circulation at Site U1357. The gyre transport is around 35 Sv, and comes
247 mainly from the Ross Sea region, with a lesser contribution from a westward flow associated with the
248 Antarctic Circumpolar Current (McCartney and Donohue, 2007).

249

250 **4.2 Site specific interpretation of $\delta^2\text{H}_{\text{FA}}$ as a glacial meltwater proxy**

251

252 **4.2.1. Source of fatty acids**

253 To best interpret the hydrogen isotope signal recorded by the C_{18} FA, it is important to determine the
254 most likely source these compounds are derived from, and thus the habitat in which they are produced.
255 The C_{18} FA, however, is known to be produced by a wide range of organisms and so we cannot preclude
256 the possibility of multiple sources, especially in a highly diverse and productive region such as the
257 surface waters of offshore Adélie Land. However, we can attempt to determine the most dominant
258 producer(s), which will help us understand the main signal being recorded by the isotopes.

259

260 An analysis of the FAs within eight classes of microalgae by Dalsgaard *et al.* (2003) (compiling results
261 from multiple studies) showed *Cryptophyceae*, *Chlorophyceae*, *Prasinophyceae* and *Prymnesiophyceae*
262 to be the most dominant producers of total C_{18} FAs. The *Bacillariophyceae* class, on the other hand,
263 which includes the diatoms, were found to produce only minor amounts of C_{18} FA, instead synthesizing
264 abundant $\text{C}_{16:1}$ FAs. Thus, despite the water column offshore Adélie Land being dominated by diatoms,
265 these are unlikely to be a major source of the C_{18} FA within U1357B (Beans *et al.*, 2008; Riaux-Gobin
266 *et al.*, 2011).

267

268 Of the four microalgae classes dominating C_{18} production (Dalsgaard *et al.*, 2003), species from the
269 Chlorophyceae and Prymnesiophyceae classes have been observed within surface waters offshore
270 Adélie Land after spring sea-ice break-up (Riaux-Gobin *et al.*, 2011). Here, *Phaeocystis antarctica* of
271 the Prymnesiophytes was found to dominate the surface water phytoplankton community (representing
272 16% of the phytoplankton assemblage), whereas Cryptophyceae spp. were found in only minor
273 abundances (Riaux-Gobin *et al.*, 2011). In the Antarctic, *Phaeocystis* is thought to be the most dominant
274 producer of C_{18} FAs (Dalsgaard *et al.*, 2003), and thus is likely to be a key producer of the C_{18} FA in
275 U1357B samples.

276

277 To investigate this further, we measured compound-specific carbon isotopes of the C₁₈ FAs in U1357B
278 samples, which gives an average δ¹³C value of -29.8 ± 1.0 ‰ (n=85). Budge *et al.* (2008) measured a
279 similar δ¹³C value of -30.7 ± 0.8‰ from C₁₆ FAs derived from Arctic pelagic phytoplankton, while sea
280 ice algae and higher trophic level organisms all had much higher δ¹³C values (sea ice algae having
281 values of -24.0 ± 2.4‰). Assuming similar values apply for the C₁₈ FA and for organisms within the
282 water column at our site, this suggests that our C₁₈ FA is predominantly derived from pelagic
283 phytoplankton.

284

285 Furthermore, δ¹³C measurements of suspended particulate organic matter (SPOM) near Prydz Bay, East
286 Antarctica by Kopczynska *et al.* (1995) showed that sites with high- δ¹³C SPOM values (-20.1 to -
287 22.4‰) were characterized by diatoms and large heterotrophic dinoflagellates, whereas the lowest δ¹³C
288 SPOM values (-29.7 to -31.85‰) were associated with *Phaeocystis*, naked flagellates and autotrophic
289 dinoflagellates. Wong and Sackett (1978) measured the carbon isotope fractionation of seventeen
290 species of marine phytoplankton and showed that Haptophyceae (of which *Phaeocystis* belongs) had the
291 largest fractionation of -35.5‰.

292

293 Therefore, based on the known producers of C₁₈ FAs, observed phytoplankton assemblages within
294 modern surface waters offshore Adélie Land, and the δ¹³C value of C₁₈ FAs in U1357B samples, as
295 discussed above, we argue that the C₁₈ FA here is predominantly produced by *Phaeocystis* (most likely
296 *P. antarctica*), but with potential minor inputs from other algal species such as Cryptophytes or diatoms.

297

298 *Phaeocystis antarctica* is a major phytoplankton species within the Antarctic, dominating spring
299 phytoplankton blooms, particularly in the Ross Sea (DiTullio *et al.*, 2000; Schoemann *et al.*, 2005). It is
300 known to exist both within sea ice and in open water (Riaux-Gobin *et al.*, 2013) and has been observed
301 in surface waters in great abundance following spring sea-ice break-up, at both coastal and offshore sites
302 in Adélie Land (Riaux-Gobin *et al.*, 2011).

303

304 Although a large proportion of organic matter produced in the surface water is recycled in the upper
305 water column, the small fraction which is deposited in the sediment reaches the sea floor through large
306 particles sinking from above as “marine snow”. This export production includes large algal cells, fecal
307 pellets, zooplankton carcasses and molts, and amorphous aggregates (Mayer, 1993). In the Ross Sea,

308 aggregates of *P. antarctica*, have been observed to sink at speeds of more than 200 m day⁻¹, meaning
309 they could reach deep water very quickly (Asper and Smith, 1999). In this way, a proportion of the lipid
310 content of *P. antarctica* and other algae is transported and sequestered in the sediments.

311

312 Initial diagenesis is characterized by the preferential degradation of more labile organic compounds e.g.
313 sugars, proteins, amino acids. Proportionally, lipids are relatively recalcitrant compared to other
314 compounds (e.g. amino acids, proteins) and thus are more likely to be preserved as molecular
315 biomarkers on geological timescales, even where the rest of the organism may be completely degraded
316 (Peters and Moldowan, 1993). The final proportion of lipids that are preserved within sediments are
317 affected by factors including the export production, O₂ content, residence time in the water column and
318 at the sediment/water interface before deposition, molecular reactivity, formation of macromolecular
319 complexes, adsorption to mineral surfaces and bioturbation (Meyers and Ishiwatari, 1993; Killops and
320 Killops, 2004). Within lacustrine sediments, a significant shift in FA distributions has been shown to
321 occur within 100 years due to early diagenesis, after which the FA distribution remains relatively
322 unaffected by diagenesis (Matsuda, 1978), thus major changes are assumed to reflect primary
323 environmental signals on longer timescales such as in our Holocene record. Due to the
324 hyperproductivity of the surface waters offshore Adélie land, we assume the dominant inputs of the C₁₈
325 FA are from algal sources in overlying waters and upcurrent regions. Allochthonous inputs e.g. long-
326 range aeolian transport of plant material are assumed to be minimal.

327

328 **4.2.2. Interpretation of hydrogen isotopes**

329 Compound-specific H isotopes of algal biomarkers are a well-used climate proxy in sediments
330 throughout the Cenozoic (e.g. Pagani *et al.*, 2006; Feakins *et al.*, 2012). Although diagenetic alteration,
331 including H-exchange, is possible within sedimentary archives, this has shown to be minimal in
332 sediments younger than 20 Ma (Sessions *et al.*, 2004). Furthermore, if H-exchange had occurred, we
333 would expect $\delta^2\text{H}$ values between different FA chain lengths and closely spaced samples to be driven
334 towards homogeneity, yet large variability remains, suggesting this is not the case. Thus, we are
335 confident that our measured H isotopes are indicating a primary signal throughout the Holocene.

336

337 The $\delta^2\text{H}$ value preserved in biomarkers is known to be correlated, but offset, with the $\delta^2\text{H}$ of the water
338 from which the hydrogen was derived. Measured $\delta^2\text{H}$ can therefore be described as a function of either
339 the $\delta^2\text{H}$ of the water source, or the fractionation occurring between source water and the lipid ($\epsilon_{l/w}$) (i.e.
340 vital effects), in which various environmental factors play a part (Sachse *et al.*, 2012).

341

342 The main environmental factors controlling $\epsilon_{l/w}$ are salinity and temperature, with which $\delta^2\text{H}$ increases
343 by 1-4‰ per increase in practical salinity unit (psu) (Schouten *et al.*, 2006; Sachse *et al.*, 2012) and
344 decreases by 2-4‰ per degree C increase (Zhang *et al.*, 2009), respectively. The $\delta^2\text{H}_{\text{FA}}$ record from Site
345 U1357 displays an absolute range of ca. 123‰, and millennial to centennial scale variability with an
346 amplitude of ca. 50‰, throughout the core. This would imply extremely large and pervasive variations
347 in temperature (up to ca. 60°C) and salinity (up to 123 psu) if fractionation driven by either of these
348 factors were the main control. One study has shown the salinity of present day Adélie shelf waters to
349 vary between 34 and 34.8 psu (Bindoff *et al.*, 2000), while tetraether-lipid based subsurface (50-200 m)
350 temperature estimates from nearby Site MD03-2601 (about 50 km west of Site U1357) range from -0.17
351 to 5.35°C over the Holocene (Kim *et al.*, 2010). Therefore, fractionation changes driven by temperature
352 or salinity cannot be invoked as a major control on $\delta^2\text{H}_{\text{FA}}$ in the Holocene.

353

354 Thus, the most parsimonious explanation relates to changes in $\delta^2\text{H}_{\text{FA}}$ of the water source (Sachse *et al.*,
355 2012). In the Adélie Basin, the most apparent controls on this are advection, upwelling or inputs of
356 isotopically depleted glacial meltwater. The $\delta^2\text{H}_{\text{FA}}$ value within Antarctic glaciers is highly depleted
357 relative to sea water due to the Rayleigh distillation process, leading to highly negative isotope values
358 for precipitation over the continent.

359

360 The glacial meltwater originating from the Ross Ice Shelf is likely to combine ice precipitated
361 throughout the Holocene and glacial period, and from both the East and West Antarctic Ice Sheets.
362 However, as noted by Shackleton and Kennett (1975) in their first oxygen isotope record of the
363 Cenozoic (see their Fig. 6), most of the ice that melts around the margin has been coastally precipitated
364 (due to higher accumulation rates). Since ice precipitated further inland has a greater residence time
365 (Shackleton and Kennett, 1975) and significantly lower accumulation rates it will contribute
366 significantly less to this signal. Thus, the ice that was melting along this margin is best represented by
367 average values of coastal ice dome records at a similar latitude to that which melted since the LGM

368 (such as TALDICE and Siple Dome) than more southerly locations. Glacial to Holocene $\delta^2\text{H}_{\text{FA}}$ values
369 from TALDICE, located on the western edge of the Ross Sea in the East Antarctic, for example, vary
370 between -276.2 and -330.3‰ (Steig *et al.*, 1998) (converted from $\delta^{18}\text{O}$ values following the global
371 meteoric water line (GMWL): $\delta^2\text{H}_{\text{FA}} = 8.13 (\delta^{18}\text{O}) + 10.8$), while values from Siple Dome on the
372 eastern edge of the Ross Sea in the West Antarctic, vary from ca. -200 to -293‰ (Brook *et al.*, 2005).
373 Taking the average of these values as a rough estimate for the meltwater gives a $\delta^2\text{H}$ value of ca. -
374 275‰. We note our calculations are based on averages of set time periods, which we expect would
375 integrate ice of various ages - rather than extreme values which could relate to specific melt events of ice
376 or biases to certain ages/regions. This seems reasonable - the isotopic signal of coastal surface waters
377 masses advected from the RIS to the Adélie land (as illustrated in Fig. 3 and 4) must integrate a range of
378 source areas across the RIS and from the coast around to Adélie Land.

379

380 In comparison to the highly negative glacial ice isotope composition, sea surface water $\delta^{18}\text{O}$
381 measurements taken near the Mertz Glacier offshore Adélie Land (140-150°E) in summer 2000-2001
382 ranged between -0.47 and 0.05‰ (Jacobs *et al.*, 2004), equivalent to $\delta^2\text{H}$ values of 6.9 to 11.2‰
383 (average = 9‰) following the GMWL. Thus, the two major hydrogen source pools (RIS glacial ice and
384 ocean water) have highly contrasting isotope values, meaning inputs of upstream glacial ice could have a
385 large effect on surface water $\delta^2\text{H}$ values in the Adélie Land region.

386

387 Taking the average glacial meltwater $\delta^2\text{H}$ value as -275‰ and the average modern Adélie surface water
388 $\delta^2\text{H}$ value of 9‰ as end-members, and assuming a biosynthetic offset between the FA and sea water of
389 173‰ (see below), we can use a simple mixing model to estimate the percentage of glacial meltwater
390 required in the surface waters to change the $\delta^2\text{H}_{\text{FA}}$ value to those recorded in U1357B samples. The
391 most negative values occur during the early Holocene, 11.4 – 8.2 ka, averaging -214.2‰ (n=18) which,
392 converted to a surface water value of -41‰, requires 17.6% of the surface water to be comprised of
393 glacial meltwater. During this time, we argue that large volumes of meltwater were reaching the core
394 site as local glaciers retreated, leading to intense surface-water stratification. Thus, a relatively high
395 percentage of meltwater in the Adélie Land surface waters seems reasonable. During the mid-Holocene
396 (5-4 ka), the average $\delta^2\text{H}_{\text{FA}}$ is very similar (-213.9‰, n=7), requiring 17.2% of the surface water to be
397 derived from glacial meltwater. During this time, we argue for the dominant meltwater source as coming

398 from the Ross Sea, and interpret this as a major period of glacial retreat (see section 5.2), during which
399 large volumes of meltwater are injected into the surface water and transported to the Adélie coast. In
400 contrast, the most recent samples (last 0.5 ka, n=7), which includes the most positive value of the record,
401 has an average $\delta^2\text{H}_{\text{FA}}$ value of -174.5‰. This brings the surface water value up to -1.5‰, which
402 approaches modern measured values, and requires just 3.7% (e.g. well within uncertainties) of the
403 surface waters in the Adélie Land to be glacial meltwater. However, it is also possible that the meltwater
404 was dominated by more LGM-aged ice. In either case, perturbation of the exact isotopic values still
405 indicate only significant changes in the flux of glacial meltwater can account for this signal. For
406 example, the use of -330‰ (LGM values) for the ice input gives an estimate of 3% of the surface water
407 being comprised of glacial meltwater for latest Holocene values, and 14.7% for pre 8 ka values. Taking -
408 240‰ (Holocene values) for the ice input gives an estimate of 4% for latest Holocene values, and 20%
409 for pre 8 ka values). Thus even with changing isotopic values though the deglacial, this signal of
410 changing meltwater flux would still dominate. We note these are semi-quantitative estimates, as the
411 salinity and temperature fractionation could reduce these estimates further (but cannot account for the
412 whole signal).

413

414 Surface water $\delta^{18}\text{O}$ values around Antarctica (below 60°S), measured between 1964 and 2006, ranged
415 from -8.52‰ to 0.42‰ (Schmidt *et al.*, 1999), the most negative value having been measured proximal
416 to the George VI Ice Shelf edge, where high melt rates have been observed (Potter and Paren, 1985). If
417 converted to $\delta^2\text{H}$ using the global meteoric water line, these values give a $\delta^2\text{H}$ range of 83.4‰. Thus,
418 our absolute $\delta^2\text{H}_{\text{FA}}$ range of 123‰ over the Holocene suggests a range of isotopically depleted
419 meltwater inputs to our core site over this time that are 1.5 times greater than that occurring in different
420 locations around the Antarctic in recent decades. This seems plausible based on geological evidence that
421 indicates large glacial retreat and ice mass loss occurred from the Ross Sea sector during the Holocene
422 (Anderson *et al.*, 2014; McKay *et al.*, 2016; Spector *et al.*, 2017), meaning resultant changes in surface
423 water are likely to be greater in magnitude than observed around the Antarctic in recent decades. This
424 assumes a relatively constant value for the isotopic composition of glacial meltwater, however, there is
425 likely to be some variability due to the possibility of melting ice of different $\delta^2\text{H}$ values. But, as
426 discussed above, the meltwater is best represented by the average values of the ice sheet, rather than
427 extreme values, since it must (over the broad expanse of the RIS) include an integrated signal, and thus
428 the actual variation in meltwater $\delta^2\text{H}$ will be significantly within the range of the end-members.

429

430 Although the biosynthetic fractionation of the C₁₈ FAs in U1357B is unknown, we assume that the offset
431 with surface water remains relatively constant throughout the record. Sessions *et al.* (1999) showed the
432 biosynthetic fractionation of hydrogen isotopes in the C₁₈ FA from four different marine algae to range
433 from -189 to -157‰. If we take the average of these values of 173‰ and apply this as a biosynthetic
434 offset to the youngest samples in U1357B (last 0.5 ka, n=7), which includes the most positive value of
435 the record, gives an average $\delta^2\text{H}_{\text{FA}}$ value of -174.5‰. This brings the surface water value up to -1.5‰,
436 which approaches modern measured values (Jacobs *et al.*, 2004).

437

438 Furthermore, it is interesting to note that the biosynthetic offsets measured by Sessions *et al.* (1999) for
439 the C₁₈ FA from different algal species have a total $\delta^2\text{H}$ range of 32‰. Although we cannot dismiss
440 changes in the relative contribution of C₁₈ from different species in U1357B samples (and thus different
441 biosynthetic fractionations), we argue this would only be a minor control on $\delta^2\text{H}$ compared to other
442 influences. As a thought experiment, taking the above end-members for biosynthetic fractionation from
443 Sessions *et al.* (1999), even with a 100% change in C₁₈ producer to a different algal source, this could
444 only explain a quarter of the observed $\delta^2\text{H}$ change (i.e. 32‰ of 123‰).

445

446 Therefore, we interpret the first order control on $\delta^2\text{H}_{\text{FA}}$ at Site U1357 as inputs of isotopically depleted
447 glacial meltwater. Such inputs are, in turn, influenced by the mass balance of the proximal or up-current
448 glaciers and ice-shelves.

449

450 4.3 Other proxies

451 Grain size, natural gamma radiation (NGR) and terrigenous and biosiliceous mass accumulation rates
452 (MARs) reflect changing sediment delivery either driven via local glacial meltwater discharge or
453 advection of suspended sediment by oceanic currents. The diene/triene HBI ratio is used as a proxy for
454 coastal sea ice presence (Massé *et al.*, 2011), in which high values indicate greater sea ice extent over
455 the core site. The HBI diene, also known as Ice Proxy for the Southern Ocean with 25 carbon atoms
456 (IPSO25), has been shown to derive from a sea-ice associated diatom (Belt *et al.*, 2016), whereas the
457 HBI triene is produced in the marginal ice zone (Smik *et al.*, 2016). Ba/Ti enrichment is considered to
458 reflect enhanced primary productivity. Interpretation of these proxies is discussed in more detail in
459 Supplementary Information S2.

460 5 RESULTS

461 5.1. Model simulations

462 We employed a series of sensitivity tests from a high-resolution numerical ocean model by releasing a
463 range of meltwater volumes (0.01 to 1 Sv) from along the front of the Ross Ice Shelf (RIS) to determine
464 its pathway. This demonstrates that, even under the lowest flux scenarios, freshwater is transported
465 anticlockwise, entrained within the coastal current (Fig. 2 and 3), and reaches Site U1357 within a year.
466 Moreover, although the higher input scenarios are not realistic values for the release of meltwater since
467 the LGM, the full range of simulations show a strong linear relationship between meltwater flux and
468 salinity change at the core site (Fig 3), suggesting the magnitude of the signal recorded at Site U1357 is
469 directly related to the magnitude of meltwater released. Thus, we argue that any changes in Ross Sea
470 water mass properties (salinity and temperature) would have a direct influence on surface water mass
471 properties at Site U1357 during the Holocene.

472 5.2 Geochemical data

473
474 The main datasets from Core U1357 are displayed in Fig (2) and S2. FA $\delta^2\text{H}$ (Fig 4a) shows an overall
475 trend towards more positive values over the course of the Holocene, indicating a decline in glacial
476 meltwater input. There is a notable deviation from this trend in the mid-Holocene involving a sustained
477 period of more negative $\delta^2\text{H}$ values, suggesting a peak in meltwater input, centred on ca. 4.4 ka. This
478 mid-Holocene deviation in FA $\delta^2\text{H}$ coincides with an increase in the HBI diene/triene ratio (Fig. 4c),
479 indicating a baseline shift in sea ice conditions whereby greater sea ice concentrations are sustained for
480 the rest of the Holocene. This is a similar pattern to the relative abundance of the *Fragilariopsis curta*
481 group (Fig 4b), a sea ice diatom group in core MD03-2601 also indicating a shift in sea ice
482 concentrations. Along the entire record, Ba/Ti ratios show persistent periodic fluctuations in marine
483 productivity, with values between 0.1 and 2.7 (Fig. 4g). A marked enrichment can be observed at ca. 4.4
484 ka reaching Ba/Ti ratio values over 36.1, suggesting a peak in primary productivity, before declining to
485 background levels again (Fig. 4g).

487 5.3 Sedimentological data

488 The stratigraphy of U1357B is divided into three units: the lowermost 10 cm recovered Last Glacial
489 Maximum (LGM) till (Unit III), overlain by 15 m of laminated mud-rich diatom oozes with ice rafted
490 debris (IRD) (Unit II), and the upper most 171 m (Unit I) consists of laminated diatom ooze with a
491 general lack of IRD and a significant reduction in terrigenous sediment (Escutia *et al.*, 2011).

492 Between ca. 11.4 and 8 ka, U1357B has a relatively high terrigenous component (i.e. high Natural Gamma
493 Radiation (NGR) content and low BSi%; Fig S4). The grain size distribution contains coarse tails of fine
494 (125-250 μm) to medium sands (250-500 μm), but only one sample contains coarse sands (>500 μm) that
495 may represent ice-berg rafted debris (IBRD). However, terrigenous content and IBRD is more common in
496 the underlying Unit II. The fine-grained sands and muds have a distribution with similar modes to overlying
497 intervals, albeit with an increase in the size of the coarse silt and very fine sand modes. There is a subtle
498 increase in sorting up core between ca. 11.4 and ca.8 ka (from very poorly to poorly sorted, Fig. 5c).

499 Between 9 and 4.5 ka, mass accumulation rates (MARs) (both biogenic and terrigenous; Fig. 5e) are
500 relatively high, albeit with millennial scale variability. However, the mean grain size and sorting of the
501 terrigenous material is relatively stable throughout the entire interval, and as with the rest of Unit I there
502 is an almost complete lack of IBRD. There is a rapid increase in mud content at 4.5 ka coincident with a
503 reduction in both the biogenic and terrigenous MARs, although the terrigenous MAR curve shows higher
504 accumulation rates than the biogenic MAR curve (Fig. 5e and f).

505

506 **6. DISCUSSION**

507

508 The sedimentology and geometry of the drift prior to ~11.4 ka (Unit II) is consistent with the calving
509 bay reentrant model (Domack *et al.*, 2006; Leventer *et al.*, 2006) (Fig. 1 and Supplementary Fig. S4;
510 Supplementary Materials), whereby LGM ice retreated in the deeper troughs while remaining grounded
511 on shallower banks and ridges. Sediment laden meltwater and IRD content in Unit II (>11.4 ka) is thus
512 likely derived from local outlet glaciers. However, anomalously old radiocarbon ages due to glacial
513 reworking precludes development of a reliable age model prior to the Holocene (Supplementary
514 Materials).

515 The results of model simulations (Section 5.1) indicate that, although several small glaciers within
516 Adélie Land may contribute meltwater to the site, the region is also likely to be influenced significantly
517 by changes in Ross Sea waters. Freshwater release simulations from the Ross Ice Shelf (RIS) confirm

518 this oceanographic continuity between the Ross Sea and the Wilkes region (Fig. 2). All five simulations
519 indicate that meltwater released from the edge of the RIS is almost completely entrained within the
520 westward coastal surface current and reaches Site U1357 within 4 months to 1 year (Fig 3). These fluxes
521 cover a wide range of meltwater inputs and show a strong linear relationship with salinity at the core site
522 (Fig. 4a). This suggests that the magnitude of the signal recorded at Site U1357 is directly related to the
523 magnitude of the meltwater input.

524 Local processes do also play a critical role in this region. For example, episodic calving events of the
525 Mertz Glacier tongue release fast ice over the drill site and create strong surface water stratification,
526 cutting off local AABW production (Campagne *et al.*, 2015). Although appearing to be only a local
527 process, there is still a regional (Ross Sea) influence, as this fast ice that builds up behind the Mertz
528 Glacier is formed by the freezing of fresher AASW transported from the Ross Sea (Fig 2). Thus,
529 conditions in the Ross Sea, such as the melting of isotopically depleted glacial ice, would influence both
530 the isotopic composition and amount of this sea ice.

531

532 **6.1 Early Holocene**

533 The base of the drift deposit shows downlapping of material suggesting a supply from the south,
534 indicating local focusing of meltwater and terrigenous material was the dominating influence until 11.4
535 ka (Supplementary Materials S2.2 and Fig. S4). This is overlain by onlapping strata (Unit I) with the
536 drift forming an east-west elongation on the northern flank of the Dumont d'Urville Trough, which is
537 more consistent with advection of material from the east than with delivery from local outlet glaciers to
538 the south. Thus, an increased meltwater influence from the Ross Sea is likely since this time.

539

540 Due to the potential for competing sources of glacial meltwater in the earliest Holocene, we focus our
541 study on Unit I, where there is less influence of calving bay processes (Escutia *et al.*, 2011). However,
542 the earliest part of Unit I (11.4 to 8 ka BP), which includes the most negative $\delta^2\text{H}_{\text{FA}}$ values, is
543 characterized by a very gradual upcore increase of sorting in the terrigenous sediment supply,
544 decreasing natural gamma ray (NGR) values (Fig. 5b and c) and a general lack of IRD (Escutia *et al.*,
545 2011). We conservatively interpret this as potentially maintaining some local glacial meltwater input
546 from local outlet glaciers in the lowermost interval of Unit I. Nevertheless, this process was probably

547 greatly reduced relative to Unit II deposition and it is likely much of this signal between 11.4 and 8 ka
548 could still be derived from water masses advecting to the site from the east (e.g. the Ross Sea).

549

550 This is supported by geological and cosmogenic evidence which demonstrates that the majority of the
551 margin of the East Antarctic, and also the Amundsen Sea margins, had retreated to their modern-day
552 positions by ~10 ka (Bentley et al., 2014; Mackintosh et al., 2014; Hillenbrand et al., 2017). Thus, these
553 margins are unlikely to contribute large scale shifts in meltwater fluxes to the Adélie Coast during most
554 of the Holocene. The history of grounding line retreat in the Ross sea is relatively well-constrained,
555 particularly in the Western Ross Sea, and the loss of residual ice caps appears to be largely complete by
556 ca. 7 ka to the immediate north of Ross Island, near present day calving line front of the Ross Ice Shelf
557 (Anderson et al., 2014; McKay et al. 2016). Indeed, the phase of isotopically depleted glacial meltwater
558 is apparent at Site U1357 between 8 and 7 ka could be sourced from the Ross Sea, reconciling our data
559 with these chronologies. Prior to 8 ka, any meltwater signal in U1357B is potentially influenced by local
560 glacier retreat, based on the caveats noted earlier in the grainsize and geophysical datasets (S2.2),
561 although we note a dominant Ross Sea contribution to this signal is possible.

562

563 Glacial retreat, however, persisted in the Ross Sea until at least 3 ka (Anderson et al., 2014; Spector et
564 al., 2017) providing a large upstream source of meltwater feeding into the Adélie Coast. We therefore
565 interpret our meltwater signal as being dominated by Ross Sea inputs since at least 8 ka, but potentially
566 as early as 11.4 ka. Furthermore, the retreat of grounded ice from the outer Ross Sea continental shelf
567 was accompanied by the growth of a significant floating ice shelf (which was not the case in the
568 Amundsen Sea or proximal East Antarctic coast) (Bentley et al., 2014).

569

570 An overall trend to more positive $\delta^2\text{H}_{\text{FA}}$ values, from the most negative value of the record at ~9.6 ka, to
571 ~8 ka indicates decreasing meltwater (Fig. 4a), thus suggesting a gradually diminished input from either
572 local outlet glaciers or the Ross Sea. This is associated with an increase in MARs, between 10 and 8 ka,
573 and is tentatively interpreted to represent the final retreat of residual ice from local bathymetric highs
574 allowing more material to advect into the drift (Fig. 5e). Although there is millennial scale variability,
575 MARs remain relatively high until 4.5 ka. However, $\delta^2\text{H}_{\text{FA}}$ and MARs show greater coherence at the
576 millennial-scale after 7 ka BP, suggesting that increased fluxes of glacial meltwater broadly

577 corresponded to stronger easterly currents, which advected biogenic and terrigenous material into the
578 drift.

579

580 **6.2 Middle Holocene**

581 A negative excursion in $\delta^2\text{H}_{\text{FA}}$ starting from 6 ka and culminating at 4.5 ka is interpreted to record a
582 period of enhanced glacial meltwater flux to the site relating to a final retreat phase of the major ice
583 sheet grounding line in the Ross Sea embayment (Fig. 65). A marked enrichment of Ba/Ti ratios also
584 occurs at 4.5 ka, reaching values of 36.1, on a background of baseline fluctuations between 0.1 and 2.7
585 (Fig. 2g), which suggests enhanced primary productivity, potentially driven by meltwater-induced
586 stratification. Ongoing Holocene retreat in the Ross Sea is interpreted to be primarily the consequence of
587 marine ice sheet instability processes resulting from the overdeepened continental shelf in that sector
588 (McKay et al., 2016). We use the model presented by Lowry et al., (2019) to help constrain the pattern
589 and rate of retreat of the grounding line to the south of Ross Island. This model compares geological
590 data with ice sheet model experiments that were forced by a range of environmental conditions. These
591 experiments indicate that the Ross Ice shelf cavity only started to expand once the grounding line
592 retreated to the south of Ross Island. Furthermore, to reconcile these model experiment with geological
593 datasets, the cavity expansion was not completed until the mid-Holocene (ca. 5 ka). This reconciles well
594 with ^{10}Be exposure ages of erratics in coastal nunataks at the confluence of the Mercer Ice Stream and
595 Reedy Glacier indicate 105 m of ice sheet deflation since 6.8 ka, with 40 m of this after 4.9 ka (Todd et
596 al., 2010), indicating the most rapid phase of retreat occurred between 6.8 ka and 4.9 ka. More recent
597 deflation profiles for the Beardmore Glacier (84°S) and Scott Glacier (86°S) regions show sustained
598 thinning between ca. 9 and 8 ka, but the Scott Glacier experience a second phase of rapid thinning of ca.
599 200 m between 6.8 and 5.3 ka (Fig. 2h), followed by a slower rate of thinning of between 5.3 and 3.5 ka
600 of ca. 100 m. Ages younger than this, near the modern surface are thought to be related to surface
601 ablation rather than dynamic thinning. This suggests that the grounding line was at its modern location
602 by ca. 3.5 ka (Spector et al., 2017) although it may have potentially retreated further south, followed by
603 a short duration readvance of the grounding line (Kingslake, et al., 2018). Glaciological evidence from
604 radar profiles suggests the development of divide flow on Roosevelt Island occurred sometime between
605 3 and 4 ka BP, suggesting that the ice sheet thickness was at least 500 m thicker until this time (Conway
606 et al., 1999). Combined, these lines of evidence suggest the majority of grounding line retreat south of
607 Ross Island occurred after 8 ka, with a sustained retreat occurring after 6.8 ka, consistent with the timing

608 of the largest inputs of glacial meltwater feeding the U1357 site. However, a younger age (e.g. 3 – 3.5
609 ka) for final establishment of the modern grounding line position is consistent with our interpretation, as
610 although the meltwater signal in $\delta^2\text{H}_{\text{FA}}$ peaks at 4.5 ka, it does not stabilise at lower levels until 3 ka.

611
612 The $\delta^2\text{H}_{\text{FA}}$ peak at 4.5 ka in U1357 coincides directly with a rapid shift in HBI biomarker ratios at the
613 site (Fig 4a and c), as well as sea ice proxies recorded in nearby site MD03-2601 (Fig. 4b), in the Ross
614 embayment (Taylor Dome ice core on a revised age model) (Steig *et al.*, 1998; Baggenstos *et al.*, 2018)
615 (Fig. 4d) and other sectors of the East Antarctic margin in Prydz Bay (JPC24) (Denis *et al.*, 2010) (Fig.
616 4e), reflecting a widespread increase in coastal sea-ice concentration and duration. We interpret
617 decreasing MAR and finer-grained terrigenous content (e.g. increased mud percent) at Site U1357 after
618 4.5 ka (Fig. 5e and f) to also be a consequence of increased coastal sea ice, reducing wind stress on the
619 ocean surface and limiting the easterly advection of detritus to the drift deposit.

620
621 Coastal sea-ice concentration and duration remain high throughout the rest of the Holocene [as recorded](#)
622 [by our HBI data \(this study Fig. 4c\); sea ice diatoms in core MD03-2601 \(Crosta *et al.*, 2008\);](#)
623 [methanesulfonic acid concentration in Taylor dome ice core](#) ~~and (Steig *et al.*, 1998); Crosta *et al.*, 2008;~~
624 [and sea ice diatoms in core JPC24 \(Denis *et al.*, 2010\)](#), compared to the period before 4.5 ka, despite a
625 decrease in glacial meltwater flux to the U1357 site. In addition, meltwater input prior to 4.5 ka does not
626 have a major influence on sea ice extent. Thus, an increase in meltwater flux cannot explain the
627 Neoglacial intensification of sea ice at ~4.5 ka. Here, we propose that greater coastal sea ice cover since
628 4.5 ka is related to the development of a large ice-shelf cavity in the Ross Sea as the ice sheet retreats
629 (Fig. 6), which pervasively modified ice shelf-ocean interactions and increased sea ice production.
630 Models suggest a large cavity on the continental shelf increases contact between basal-ice and
631 circulating ocean water, driving the formation of a cool, fresh water mass feeding into the AASW,
632 stabilizing the water column and enhancing the production of sea ice (Hellmer, 2004) (Fig. 6). However,
633 under small cavities such as in the modern Amundsen Sea influenced by warm-water incursions, ice
634 shelf melting results in an “ice pump” enhancement of sub-ice shelf circulation. This increases flow of
635 warm Circumpolar Deep Water (CDW) under the ice shelf that is 100-500 times the rate of melt, and
636 this volume of water does not allow for supercooling. Small cavity ice shelf outflows are therefore warm
637 and act to restrict sea ice at the ice shelf front (Jourdain *et al.*, 2017). Thus, during the Holocene, the size
638 of the cavity must have reached a threshold after which this positive warming feedback switched to a

639 negative feedback. We argue that such a tipping point takes place at 4.5 ka BP, when our proxy data
640 suggest meltwater peaks, and would explain why the increase in sea-ice concentration appears rapid and
641 only occurs at the peak of the meltwater input, and not during its prior increase, or previous meltwater
642 inputs (Fig. 4a-g).

643
644 Although the glacial meltwater volume is greatly reduced after 4.5 ka BP, the volume of Ice Shelf Water
645 (ISW) produced beneath the modern RIS is estimated at 0.86 Sv-1.6 Sv (Holland *et al.*, 2003; Smethie
646 and Jacobs, 2005). We note that ISW is not glacial meltwater, but it is defined as a supercooled water
647 mass formed through interaction with the base of the RIS, but once formed acts to modify other water
648 masses in the Ross Sea. A significant proportion of ISW is high salinity and is thus advected northwards
649 at intermediate waters depth to ultimately form AABW. However, a significant volume of ISW is lower
650 salinity and buoyant, due to development of frazil ice, and acts to mixes with surface waters (Robinson
651 *et al.*, 2014). Currently, a 0.4 Sv plume of ISW in the western margin of the Ross Ice Shelf (Robinson *et al.*,
652 2014) is directly delivered to the surface resulting in enhanced sea ice production, while seasonal
653 melt of this enhanced sea ice further acts to cool and freshen surface waters. Although unrealistic in the
654 context of a post-LGM meltwater flux from the Ross Sea alone, the larger meltwater release scenarios in
655 our simulations (0.5 to 1 Sv) show the potential pathways that a cool, fresher surface water mass
656 collecting and forming on the broad Ross Sea continental shelf would follow (Fig. 2b). These waters are
657 transported in easterly coastal currents to the Weddell Sea and the Antarctic Peninsula. This eventually
658 retroflects to join the Antarctic Circumpolar Current (Fig. 2b), and thus has potential for cooling and
659 freshening in the South Atlantic far offshore, as the ice shelf cavity increased in the Ross Sea. Indeed,
660 offshore site ODP 1094 records increased lithics in the South Atlantic after 4.5 ka (Fig. 4f), relative to
661 the period before, suggested to have been predominantly transported by sea ice indicating a cooling in
662 sea surface temperatures and increase in sea-ice extent in the South Atlantic at this time (Hodell *et al.*,
663 2001; Nielsen *et al.*, 2007). However, it also is feasible that this circum-Antarctic cooling signal
664 indicates similar melt processes may have been occurring in the Weddell Sea at ~4.5 ka, as suggested by
665 cosmogenic nuclide data (Hein *et al.*, 2016).

666

667 **6.3 What Drove the Neoglacial Transition?**

668 Our observed coastal sea-ice increase is part of a widespread transition to Neoglacial conditions both
669 globally and at high southern latitudes (Kim *et al.*, 2002; Masson-Delmotte *et al.*, 2011; Marcott *et al.*,

670 2013; Solomina *et al.*, 2015). However, most current climate models do not simulate this cooling trend,
671 resulting in a significant data-model mismatch (Liu *et al.*, 2014) ([Supplementary-Fig. 7S6](#)). Marine ice
672 sheet retreat along the Pacific margin of West Antarctic has previously been proposed to be triggered by
673 enhanced wind-driven incursions of warm CDW onto the continental shelves in the early Holocene
674 (Hillenbrand *et al.*, 2017), with continued retreat in the Ross Sea being the consequence of the
675 overdeepened continental shelf and marine ice sheet instability processes (McKay *et al.*, 2016). We
676 propose that a series of negative feedbacks was also associated with the latter phases of this retreat due
677 to the RIS cavity expansion that occurred in the mid-Holocene, with similar processes possibly
678 occurring in the Weddell Sea, leading to the onset and continuation of Neoglacial conditions.
679 Widespread albedo changes associated with increased coastal sea ice would have amplified regional
680 cooling trends (Masson-Delmotte *et al.*, 2011), whilst increased stratification resulting from seasonal
681 sea-ice melt and increased ISW production drove the deepening of the fresher water surface isopycnal at
682 the continental shelf break. Grounding line retreat creates new space for continental shelf water masses
683 to form, while ice shelf cavity expansion promotes supercooling of waters circulating beneath the ice
684 shelf, and freshening of AASW. Thus, as seasonal sea ice melt and ice shelf supercooling processes
685 played a greater role in enhancing AASW cooling and production on the continental shelf, they would
686 have acted to restrict warmer subsurface water transport onto the continental shelf (Smith Jr. *et al.*,
687 2012) (Fig. [6S](#)). Furthermore, the Neoglacial sea-ice increase itself may have been associated with a
688 stabilising feedback mechanism (which also is not resolved in ice-ocean models) through its role in
689 dampening ocean-induced wave flexural stresses at ice shelf margins, reducing their vulnerability to
690 catastrophic collapse (Massom *et al.*, 2018). We suggest that some combination of the above processes
691 could have acted to slow the rate of Ross Sea grounding line retreat and reduced basal ice shelf melt as
692 indicated by a trend towards more positive $\delta^2\text{H}_{\text{FA}}$ values in U1357 between 4.5 and 3 ka (Fig. 4a).
693 Furthermore, large Antarctic ice shelves currently have large zones of marine accreted ice resulting from
694 supercooling (Rignot *et al.*, 2013), thus the signature of $\delta^2\text{H}_{\text{FA}}$ is anticipated to become more positive as
695 the ice shelf approaches a steady state of mass balance, relative to the thinning phases when basal melt
696 rates exceed that of accretion. The stabilization of $\delta^2\text{H}_{\text{FA}}$ values observed at 3 ka in U1357 suggests the
697 Ross Ice Shelf has maintained a relatively steady state of mass balance since this time.

698

699 A recent study implies that the late Holocene shift in [patterns of](#) coastal versus open water sea ice
700 patterns in the Ross Sea was driven an increase in katabatic winds since at least 3.6 ka in the Ross Sea

701 (Mezgec *et al.*, 2017), leading to enhanced polynya activity. During colder Antarctic climates, increased
702 latitudinal temperature gradients enhanced katabatic winds in the Ross Sea (Rhodes *et al.*, 2012). This is
703 consistent with our hypothesis, as we interpret this katabatic wind and polynya activity signal to be a
704 response to the preceding Neoglacial cooling at 4.5 ka and evolution of the modern ocean-ice shelf
705 connectivity, which our data suggest was primarily driven by ice shelf cavity expansion. Furthermore,
706 this transition takes place on the background of declining winter insolation (Berger and Loutre, 1991)
707 which would have acted to further enhance and maintain these changes. This insolation decline has
708 previously been hypothesised as a driver of the Neoglacial increase in coastal sea ice in both Prydz Bay
709 and the Adélie Land regions (Denis *et al.*, 2010), however this monotonic decrease contrasts with the
710 markedly rapid increase in sea ice observed in many records (Fig 2). Our mechanism of ice shelf cavity
711 expansion, reaching a threshold that promoted significant supercooling of continental shelf water
712 masses, reconciles both the rapidity and timing of Neoglacial onset in the middle Holocene.

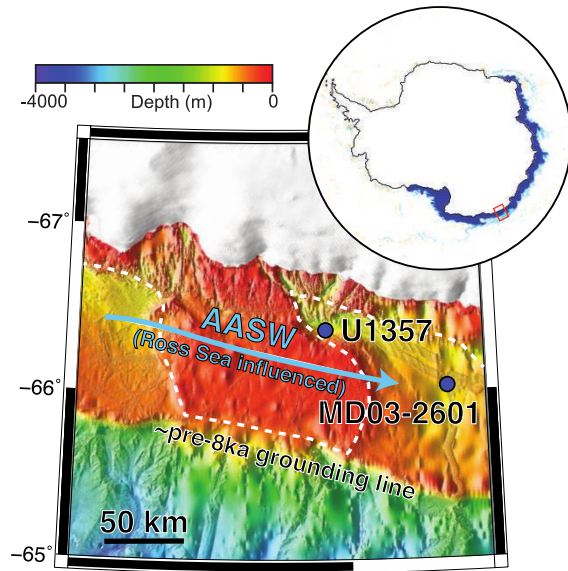
713

714 **7. Conclusions and Implications for Antarctic Climate, Sea-Ice and Ice Shelf Behaviour**

715 Our multiproxy record of changing oceanographic conditions in the Adélie Land region indicates a
716 significant meltwater event during the middle Holocene. Comparison of this record with pre-existing
717 studies from around the Antarctic margin indicates this was likely associated with final phases of
718 deglaciation of the Ross Sea embayment. Expansion of the Ross Ice Shelf cavity at this time is proposed
719 to have led to modification of surface water masses formation processes on the continental shelves of
720 Ross Sea and Adélie Land and contributed to widespread Antarctic surface water cooling and increased
721 coastal sea ice during the late Holocene Neoglacial. The lack of these coupled ice-ocean processes is
722 apparent in recent Earth system model experiments, in particular the incorporation of evolving ice shelf
723 cavities, with Trace-21k for example, instead simulating a decrease in Antarctic sea-ice extent and
724 thickness after 5 ka (Supplementary-Fig. 7S6). These model outputs are in direct contrast to multiple
725 lines of proxy data in this study and previous work (Steig *et al.*, 1998; Crosta *et al.*, 2008; Denis *et al.*,
726 2010). Consequently, our results provide insights into the magnitude of this data-model mismatch, as
727 well as a mechanism for rapid sea-ice change and grounding line stabilisation on the background of a
728 warming climate (Liu *et al.*, 2014), both on modern and Holocene time scales. Better representation of
729 the role of evolving ice shelf cavities on oceanic water mass evolution and sea-ice dynamics, which our
730 data indicate acted as a strong negative feedback, will be fundamental to understanding the
731 oceanographic and glaciological implications of future ice shelf loss in the Antarctic.

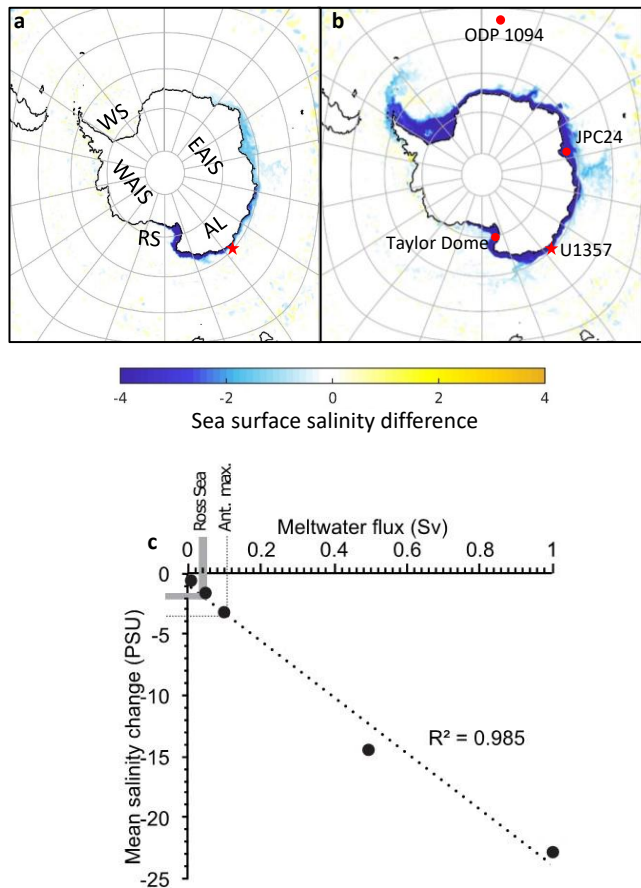
732
733
734
735
736

Figures



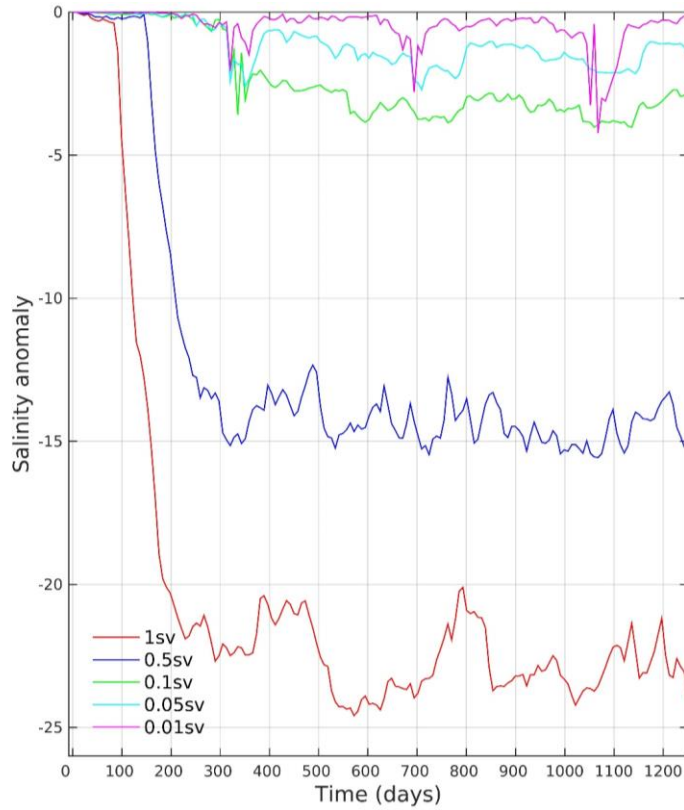
737
738
739
740
741
742
743
744
745
746

Figure 1: Location of Sites U1357 and MD03-2601 (blue dots). The ice sheet grounding line formed a calving-bay environment (dashed white line) prior to 11.4 ka, but since at least 8.2 ka Antarctic Surface Water flow is largely advected from the Ross Sea (blue line). Inset map: pathway of freshwater (dark blue) after 1 year of 1 Sv meltwater released from along the edge of the Ross Ice Shelf in a model simulation.

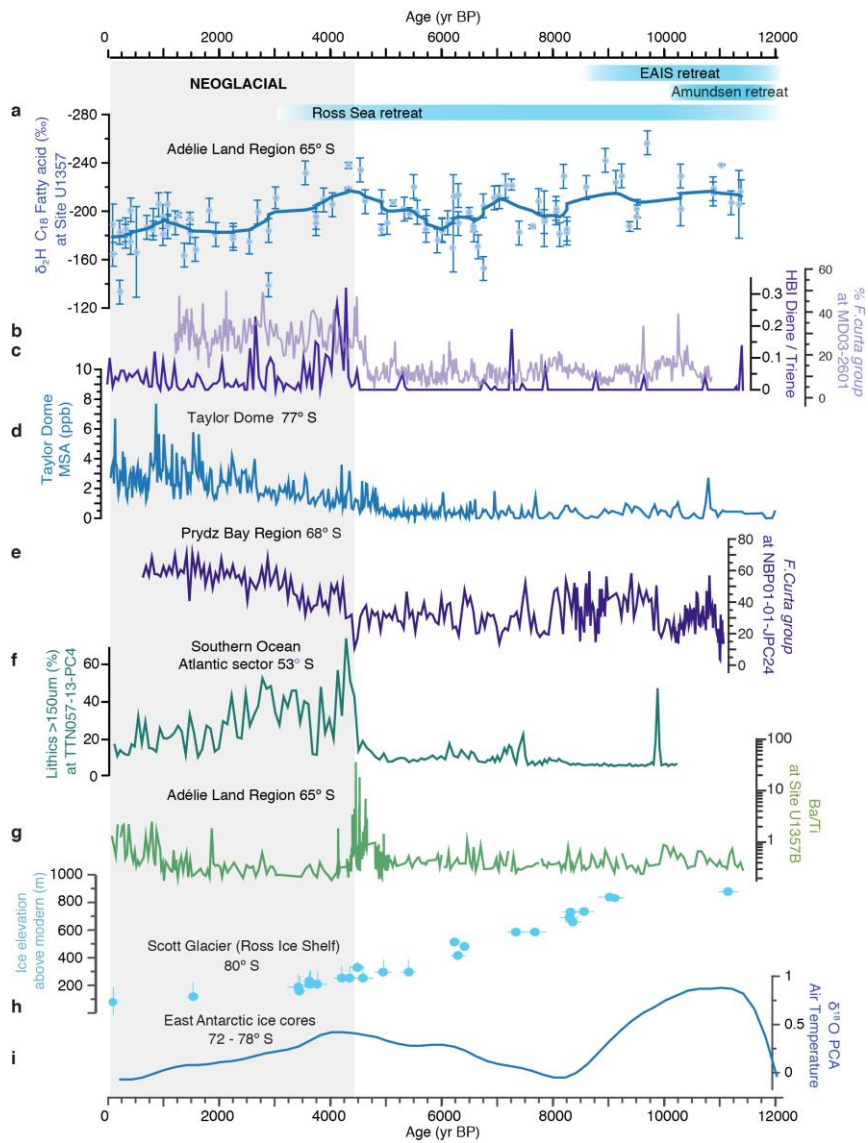


747 **Figure 2: MITgcm simulations of meltwater release from along the edge of the Ross Ice Shelf.** First
 748 two images show sea-surface salinity difference (in practical salinity units) after 3.5 model years
 749 resulting from meltwater release volumes of a) 0.1 Sv (2×10^{13} m³ total ice volume equivalent) and b) 0.5
 750 Sv (1×10^{14} m³ total ice volume equivalent). Red star indicates position of Site U1357 (this study) and
 751 red dots show positions of other core sites mentioned in this study where a Mid-Holocene increase in sea
 752 ice and/or cooling is recorded: Taylor Dome (Steig *et al.*, 1998; Baggenstos *et al.*, 2018), JPC24 (Denis
 753 *et al.*, 2010) and ODP 1094 (Nielsen *et al.*, 2007). AL = Adélie Land, RS = Ross Sea, WS = Weddell
 754 Sea, EAIS = East Antarctic Ice Sheet, WAIS = West Antarctic Ice Sheet. c) Scatter plot of simulated
 755 meltwater flux (Sv) against mean salinity difference at U1357 core site. Grey band indicates range of

756 plausible Holocene to deglacial Ross Sea meltwater inputs. Dotted line indicates maximum Antarctic
757 meltwater during the Holocene.



780 **Figure 3** Simulated salinity anomalies over time at Site U1357 for the five meltwater release
781 experiments.



790

791 **Figure 4: Holocene Adélie Land proxy records from IODP Site U1357 and other circum-Antarctic**

792 **sites.** Glacial retreat chronologies are shown as bars at the top as discussed in the text. a) $\delta^2\text{H}$ C_{18} fatty

793 acid at Site U1357 (errors bars based on replicates), with robust locally weighted smoothing (rlo wss). b)

794 *Fragilariopsis curta* group (*F. curta* and *F. cylindrus*) relative abundance at MD03-2601, as a proxy of
795 sea-ice conditions (Crosta *et al.*, 2008) c) di-unsaturated HBI (C_{25:2}; Diene)/tri-unsaturated HBI isomer
796 (C_{25:3}; Triene) ratio at Site U1357 d) Methanesulfonate (MSA) concentrations (ppb) from Taylor Dome
797 ice core e) *F. curta* group relative abundances in core NBP-01-JPC24 f) Coarse lithic (ice-rafted)
798 content at TTN057-13-PC4 (Hodell *et al.*, 2001) g) Ba/Ti (logarithmic scale) at Site U1357 h) ¹⁰Be
799 cosmogenic nuclide ages from Scott Glacier in the SW Ross Ice Shelf region (Spector *et al.*, 2017) i)
800 Temperature signal from principal component analyses of five δ¹⁸O records in five East Antarctic ice
801 cores (Vostok, EPICA Dome C, EPICA Dronning Maud Land, Dome Fuji and Talos Dome) (Masson-
802 Delmotte *et al.*, 2011).

803
804
805
806
807
808
809
810
811
812
813
814
815
816
817
818
819
820
821
822
823
824
825
826
827
828
829

830
831
832
833
834
835
836
837
838
839
840
841
842
843
844
845
846
847
848
849
850
851
852
853
854

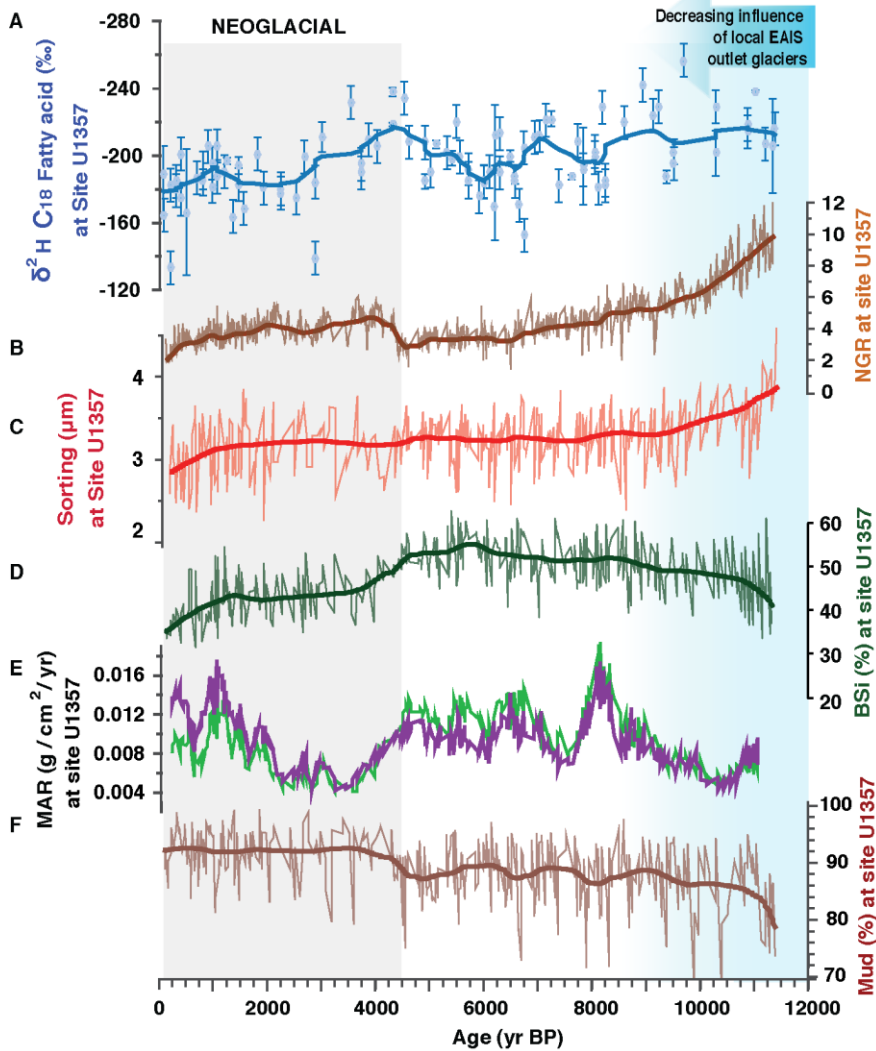
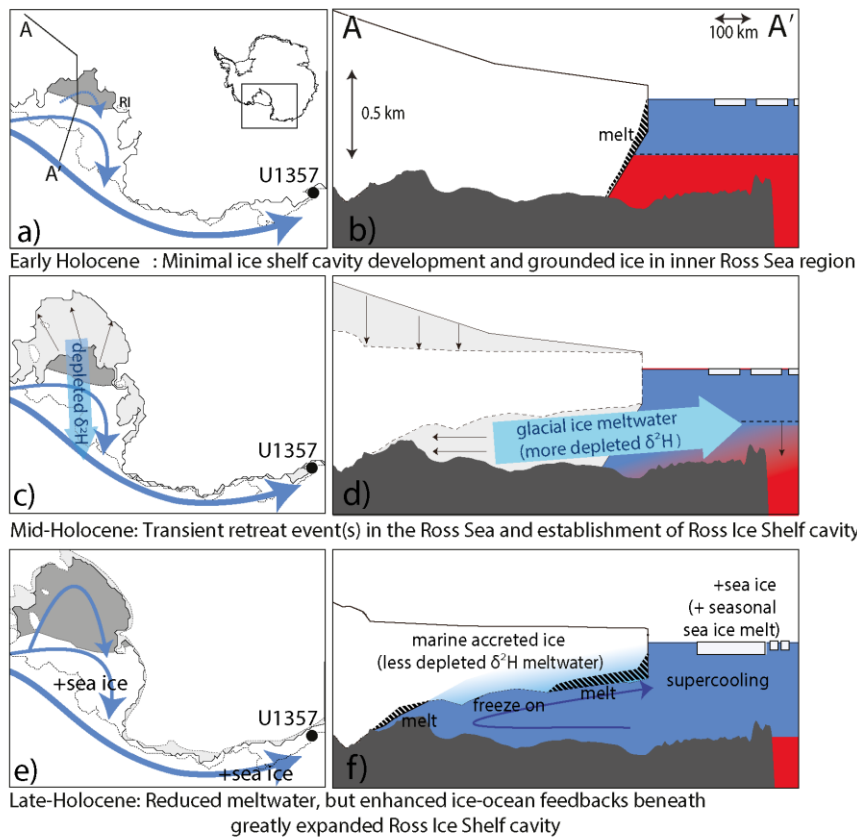


Figure 5 Holocene Adélie Land proxy records from IODP Site U1357 a) C₁₈ fatty acid $\delta^2\text{H}$ (errors bars based on replicate analyses), heavy line is a robust locally weighted scatterplot smoothing (rlowss) b) Natural Gamma Radiation, heavy line is a rowss c) grain sorting (μm) calculated following Folk and Ward (1957), heavy line is a rowss d) Percentage of biogenic silica (BSi), heavy line is a rowss; e) Mass accumulation rates of biogenic (green line) and terrigenous (purple line) material f) Percentage of mud, heavy line is a rowss.



855

856 **Figure 6: Conceptual model of evolving Holocene glacial and oceanographic conditions in the Ross**
 857 **Sea region.** Panels on the left show modelled grounding line positions (McKay *et al.*, 2016), and
 858 proposed circulation of surface and sub-ice shelf circulating waters (light blue arrows). Panels on the
 859 right show cross sections of the Ross Ice Shelf (RIS) and ice-ocean interactions. Dark blue = cool
 860 surface waters, Red = warm subsurface waters. a) The grounding line in Adélie Land is near its modern
 861 location, but near Ross Island (RI) in the Ross Sea, and ice shelf cavity (dark grey shading) is reduced in
 862 size relative to today (McKay *et al.*, 2016). b) Continental shelf profile A-A' (panel a) shows a Ross Sea
 863 grounding line in a mid-continental shelf location in close proximity to the RIS calving line (McKay *et*
 864 *al.*, 2016), with subsurface warming on the continental shelf triggering WAIS deglaciation (Hillenbrand

865 *et al.*, 2017). c) Most grounding line retreat south of RI occurred between 9 and 4.5 ka (light grey
866 shading with black arrows represents area of retreat over this period), proposed to be the consequence of
867 marine ice sheet instability, but the ice shelf calving line remained near its present position (McKay *et*
868 *al.*, 2016; Spector *et al.*, 2017). d) Grounding line retreat and ice shelf thinning released meltwater with
869 negative $\delta^2\text{H}$ into the surface waters. Increasing ice shelf-oceanic interactions with the development of
870 the ice shelf cavity (dark grey) led to enhanced Antarctic Surface Water formation; f) Minimal
871 grounding line retreat has occurred since 4.5 ka, and the RIS supercools AASW leading to enhanced
872 sea-ice formation despite reduced glacial meltwater flux. Seasonal sea ice meltwater further freshens and
873 cools AASW. Increased production of AASW on the continental shelf leads to isopycnal deepening
874 (dotted line) and limits flow onto the continental shelf slowing further grounding line retreat. However,
875 as the ice shelf is near steady state mass balance and there is a component of marine accreted ice at the
876 base of the ice shelf (Rignot *et al.*, 2013), the strength of the $\delta^2\text{H}$ signal is reduced relative to periods of
877 mass balance loss.

878

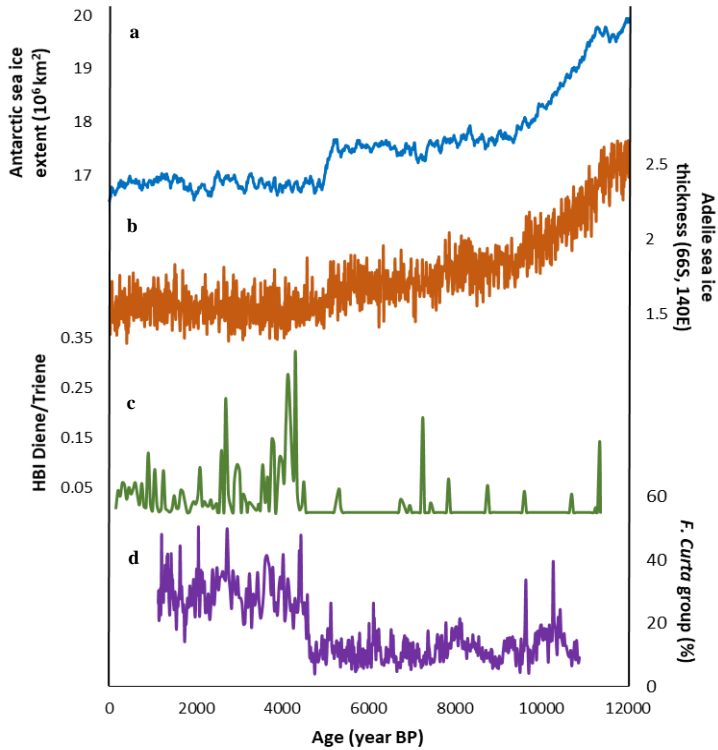


Figure S67 Comparison of sea ice data from the Adélie region with TraCE-21k simulations a) Antarctic sea ice extent (10^6 km^2) from TraCE-21k b) Adélie sea ice thickness (66°S , 140°E) from TraCE-21k c) Ratio of the di-unsaturated HBI (C25:2; Diene) and the tri-unsaturated HBI isomer (C25:3; Triene) at Site U1357 d) *Fragilariopsis curta* group relative abundances from MD03-2601.

Formatted: Font: 12 pt

Formatted: Left

880
881
882

References:

- 883 Adcroft, A. *et al.* (2004) 'Implementation of an Atmosphere–Ocean General Circulation Model on the
884 Expanded Spherical Cube', *Monthly Weather Review*, 132(12), pp. 2845–2863. doi:
885 10.1175/MWR2823.1.
- 886 Anderson, J. B. *et al.* (2014) 'Ross Sea paleo-ice sheet drainage and deglacial history during and since
887 the LGM', *Quaternary Science Reviews*. Elsevier Ltd, 100, pp. 31–54. doi:
888 10.1016/j.quascirev.2013.08.020.
- 889 Aoki, S. *et al.* (2013) 'Widespread freshening in the Seasonal Ice Zone near 140°E off the Adélie Land

890 Coast, Antarctica, from 1994 to 2012', *Journal of Geophysical Research: Oceans*, 118(11), pp. 6046–
891 6063. doi: 10.1002/2013JC009009.

892 Arrigo, K. R. and van Dijken, G. L. (2003) 'Phytoplankton dynamics within 37 Antarctic coastal
893 polynya systems', *Journal of Geophysical Research*, 108(C8), p. 3271. doi: 10.1029/2002JC001739.

894 Asper, V. L. and Smith, W. O. (1999) 'Particle fluxes during austral spring and summer in the southern
895 Ross Sea, Antarctica', *Journal of Geophysical Research: Oceans*, 104(C3), pp. 5345–5359. doi:
896 10.1029/1998JC900067.

897 Baggenstos, D. *et al.* (2018) 'A Horizontal Ice Core From Taylor Glacier, Its Implications for Antarctic
898 Climate History, and an Improved Taylor Dome Ice Core Time Scale', *Paleoceanography and
899 Paleoclimatology*, 33(7), pp. 778–794. doi: 10.1029/2017PA003297.

900 Beans, C. *et al.* (2008) 'A study of the diatom-dominated microplankton summer assemblages in coastal
901 waters from Terre Adelie to the Mertz Glacier, East Antarctica (139°E–145°E)', *Polar Biology*, 31(9),
902 pp. 1101–1117. doi: 10.1007/s00300-008-0452-x.

903 Belt, S. T. *et al.* (2007) 'A novel chemical fossil of palaeo sea ice: IP25', *Organic Geochemistry*, 38(1),
904 pp. 16–27. doi: 10.1016/j.orggeochem.2006.09.013.

905 Belt, S.T., Smik, L., Brown, T.A., *et al.* (2016) Source identification and distribution reveals the
906 potential of the geochemical Antarctic sea ice proxy IPSO25. *Nature Communications*, 7: 12655.
907 doi:10.1038/ncomms12655.

908 Bentley, M. J. *et al.* (2014) 'A community-based geological reconstruction of Antarctic Ice Sheet
909 deglaciation since the Last Glacial Maximum', *Quaternary Science Reviews*, 100, pp. 1–9. doi:
910 10.1016/j.quascirev.2014.06.025.

911 Berger, A. and Loutre, M. F. (1991) 'Insolation values for the climate of the last 10 million years',
912 *Quaternary Science Reviews*, 10(4), pp. 297–317. doi: 10.1016/0277-3791(91)90033-Q.

913 Bindoff, N., Rintoul, S. and Massom, R. (2000) 'Bottom water formation and polynyas in Adelie Land,
914 Antarctica', *Papers and Proceedings of the Royal Society of Tasmania*, 133(3), pp. 51–56. doi:
915 10.26749/rstpp.133.3.51.

916 Brook, E. J. *et al.* (2005) 'Timing of millennial-scale climate change at Siple Dome, West Antarctica,
917 during the last glacial period', *Quaternary Science Reviews*, 24(12–13), pp. 1333–1343. doi:
918 10.1016/j.quascirev.2005.02.002.

919 Budge, S. M. *et al.* (2008) 'Tracing carbon flow in an arctic marine food web using fatty acid-stable
920 isotope analysis', *Oecologia*, 157(1), pp. 117–129. doi: 10.1007/s00442-008-1053-7.

921 Campagne, P. *et al.* (2015) 'Glacial ice and atmospheric forcing on the Mertz Glacier Polynya over the
922 past 250 years', *Nature Communications*, 6. doi: 10.1038/ncomms7642.

923 Condron, A. and Winsor, P. (2012) 'Meltwater routing and the Younger Dryas', *Proceedings of the
924 National Academy of Sciences*, 109(49), pp. 19928–19933. doi: 10.1073/pnas.1207381109.

- 925 Conway, H., Hall, B.L., Denton, G.H., et al. (1999) Past and Future Grounding-Line Retreat of the West
926 Antarctic Ice Sheet. *Science*, 286 (5438): 280–283. doi:10.1126/science.286.5438.280.
- 927 Crosta, X., Denis, D. and Ther, O. (2008) ‘Sea ice seasonality during the Holocene, Adelie Land, East
928 Antarctica’, *Marine Micropaleontology*, 66(3–4), pp. 222–232. doi: 10.1016/j.marmicro.2007.10.001.
- 929 Dalsgaard, J. et al. (2003) ‘Fatty acid trophic markers in the pelagic marine environment’, *Advances in
930 Marine Biology*, 46, pp. 225–340. doi: 10.1016/S0065-2881(03)46005-7.
- 931 DeMaster, D. J. (1981) ‘The supply and accumulation of silica in the marine environment’, *Geochimica
932 et Cosmochimica Acta*, 45(10), pp. 1715–1732. doi: 10.1016/0016-7037(81)90006-5.
- 933 Denis, D. et al. (2010) ‘Sea ice and wind variability during the Holocene in East Antarctica: Insight on
934 middle-high latitude coupling’, *Quaternary Science Reviews*, 29(27–28), pp. 3709–3719. doi:
935 10.1016/j.quascirev.2010.08.007.
- 936 DiTullio, G. R. et al. (2000) ‘Rapid and early export of Phaeocystis antarctica blooms in the Ross Sea,
937 Antarctica’, *Nature*, 404(6778), pp. 595–598. doi: 10.1038/35007061.
- 938 Domack, E. et al. (2006) ‘Subglacial morphology and glacial evolution of the Palmer deep outlet
939 system, Antarctic Peninsula’, *Geomorphology*, 75(1–2 SPEC. ISS.), pp. 125–142. doi:
940 10.1016/j.geomorph.2004.06.013.
- 941 Escutia, C. et al. (2011) ‘Expedition 318 summary’, in. doi: 10.2204/iodp.proc.318.101.2011.
- 942 Etourneau, J. et al. (2013) ‘Holocene climate variations in the western Antarctic Peninsula: Evidence for
943 sea ice extent predominantly controlled by changes in insolation and ENSO variability’, *Climate of the
944 Past*, 9(4), pp. 1431–1446. doi: 10.5194/cp-9-1431-2013.
- 945 Feakins, S. J., Warny, S. and Lee, J.-E. (2012) ‘Hydrologic cycling over Antarctica during the middle
946 Miocene warming’, *Nature Geoscience*, 5. doi: 10.1038/NGEO1498.
- 947 Hein, A. S. et al. (2016) ‘Mid-Holocene pulse of thinning in the Weddell Sea sector of the West
948 Antarctic ice sheet’, *Nature Communications*. Nature Publishing Group, 7, p. 12511. doi:
949 10.1038/ncomms12511.
- 950 Hellmer, H. H. (2004) ‘Impact of Antarctic ice shelf basal melting on sea ice and deep ocean properties’,
951 *Geophysical Research Letters*, 31(10), pp. 1–4. doi: 10.1029/2004GL019506.
- 952 Hillenbrand, C. D. et al. (2017) ‘West Antarctic Ice Sheet retreat driven by Holocene warm water
953 incursions’, *Nature*, 547(7661), pp. 43–48. doi: 10.1038/nature22995.
- 954 Hodell, D. A. et al. (2001) ‘Abrupt Cooling of Antarctic Surface Waters and Sea Ice Expansion in the
955 South Atlantic Sector of the Southern Ocean at 5000 cal yr B.P.’, *Quaternary Research*, 56(02), pp.
956 191–198. doi: 10.1006/qres.2001.2252.
- 957 Holland, D. M., Jacobs, S. S. and Jenkins, A. (2003) ‘Modelling the ocean circulation beneath the Ross
958 Ice Shelf’, *Antarctic Science*, 15(1), pp. 13–23. doi: 10.1017/S0954102003001019.

- 959 Huang, Y. *et al.* (1999) 'Glacial-interglacial environmental changes inferred from molecular and
960 compound-specific $\delta^{13}\text{C}$ analyses of sediments from Sacred Lake, Mt. Kenya', *Geochimica et*
961 *Cosmochimica Acta*, 63(9), pp. 1383–1404. doi: 10.1016/S0016-7037(99)00074-5.
- 962 Hughes, K. *et al.* (2014) 'Extension of an Ice Shelf Water plume model beneath sea ice with application
963 in McMurdo Sound, Antarctica', *Journal of Geophysical Research: Oceans*, 119, pp. 8662–8687. doi:
964 10.1002/2014JC010248. Received.
- 965 Jacobs, S. S. *et al.* (2004) *Summer Oceanographic Measurements near the Mertz Polynya (140–150E)*
966 *on NB Palmer Cruise 00-08*. doi: 10.15784/601161.
- 967 Jacobs, S. S., Giulivi, C. F. and Mele, P. A. (2002) 'Freshening of the Ross Sea During the Late 20th
968 Century', *Science*, 297(5580), pp. 386–389. doi: 10.1126/science.1069574.
- 969 Jensen, S., Renberg, L. and Reutergrårdh, L. (1977) 'Residue Analysis of Sediment and Sewage Sludge
970 for Organochlorines in the Presence of Elemental Sulfur', *Analytical Chemistry*, 49(2), pp. 316–318.
971 doi: 10.1021/ac50010a033.
- 972 Johns, L. *et al.* (1999) 'Identification of a C₂₅ highly branched isoprenoid (HBI) diene in Antarctic
973 sediments, Antarctic sea-ice diatoms and cultured diatoms', *Organic Geochemistry*, 30(11), pp. 1471–
974 1475. doi: 10.1016/S0146-6380(99)00112-6.
- 975 Jones, J. M. *et al.* (2016) 'Assessing recent trends in high-latitude Southern Hemisphere surface
976 climate', *Nature Climate Change*. Nature Publishing Group, 6(10), pp. 917–926. doi:
977 10.1038/nclimate3103.
- 978 Jourdain, N. C. *et al.* (2017) 'Ocean circulation and sea-ice thinning induced by melting ice shelves in
979 the Amundsen Sea', *Journal of Geophysical Research: Oceans*, 122(3), pp. 2550–2573. doi:
980 10.1002/2016JC012509. Received.
- 981 Killops, S. and Killops, V. (2004) *Introduction to Organic Geochemistry*, Blackwell Publishing Ltd. doi:
982 10.1002/9781118697214.
- 983 Kim, J. H. *et al.* (2002) 'Interhemispheric comparison of deglacial sea-surface temperature patterns in
984 Atlantic eastern boundary currents', *Earth and Planetary Science Letters*, 194(3–4), pp. 383–393. doi:
985 10.1016/S0012-821X(01)00545-3.
- 986 Kim, J. H. *et al.* (2010) 'New indices and calibrations derived from the distribution of crenarchaeal
987 isoprenoid tetraether lipids: Implications for past sea surface temperature reconstructions', *Geochimica*
988 *et Cosmochimica Acta*, 74(16), pp. 4639–4654. doi: 10.1016/j.gca.2010.05.027.
- 989 Kingslake, J., Scherer, R.P., Albrecht, T., *et al.* (2018) Extensive retreat and re-advance of the West
990 Antarctic Ice Sheet during the Holocene. *Nature*, 558 (7710): 430–434. doi:10.1038/s41586-018-0208-x.
- 991 Kocczynska, E. E. *et al.* (1995) 'Phytoplankton Composition and Cell Carbon Distribution in Prydz
992 Bay, Antarctica - Relation To Organic Particulate Matter and Its Delta-C-13 Values', *Journal of*
993 *Plankton Research*, 17(4), pp. 685–707. doi: 10.1093/plankt/17.4.685.

- 994 Kusahara, K., Hasumi, H. and Tamura, T. (2010) 'Modeling sea ice production and dense shelf water
995 formation in coastal polynyas around East Antarctica', *Journal of Geophysical Research: Oceans*,
996 115(10), p. C10006. doi: 10.1029/2010JC006133.
- 997 Leventer, A. *et al.* (2006) 'Marine sediment record from the East Antarctic margin reveals dynamics of
998 ice sheet recession', *GSA Today*, 16(12), pp. 4–10. doi: 10.1130/GSAT01612A.1.
- 999 Liu, Z. *et al.* (2014) 'The Holocene temperature conundrum', *Proceedings of the National Academy of
1000 Sciences*, 111(34), pp. E3501–E3505. doi: 10.1073/pnas.1407229111.
- 1001 Lowry, D. P. *et al.* (2019) 'Deglacial grounding-line retreat in the Ross Embayment, Antarctica,
1002 controlled by ocean and atmosphere forcing', *Science Advances*. doi: 10.1126/sciadv.aav8754.
- 1003 Mackintosh, A. N. *et al.* (2014) 'Retreat history of the East Antarctic Ice Sheet since the Last Glacial
1004 Maximum', *Quaternary Science Reviews*. Elsevier Ltd, 100, pp. 10–30. doi:
1005 10.1016/j.quascirev.2013.07.024.
- 1006 Marcott, S. a. *et al.* (2013) 'A Reconstruction of Regional and Global Temperature for the Past 11,300
1007 Years', *Science (New York, N.Y.)*, 339(6124), pp. 1198–1201. doi: 10.1126/science.1228026.
- 1008 Marshall, J. *et al.* (1997) 'A finite-volume, incompressible Navier Stokes model for studies of the ocean
1009 on parallel computers', *Journal of Geophysical Research: Oceans*, 102(C3), pp. 5753–5766. doi:
1010 10.1029/96JC02775.
- 1011 Marsland, S. J. *et al.* (2004) 'Modeling water mass formation in the Mertz Glacier Polynya and Ad??lie
1012 Depression, East Antarctica', *Journal of Geophysical Research: Oceans*, 109(11), p. C11003. doi:
1013 10.1029/2004JC002441.
- 1014 Massé, G. *et al.* (2011) 'Highly branched isoprenoids as proxies for variable sea ice conditions in the
1015 Southern Ocean', *Antarctic Science*, 23(5), pp. 487–498. doi: 10.1017/S0954102011000381.
- 1016 Massom, R. A. *et al.* (2001) 'Effects of regional fast-ice and iceberg distributions on the behaviour of
1017 the Mertz Glacier polynya, East Antarctica', *Annals of Glaciology*, 33, pp. 391–398. doi:
1018 10.3189/172756401781818518.
- 1019 Massom, R. A. *et al.* (2018) 'Antarctic ice shelf disintegration triggered by sea ice loss and ocean swell',
1020 *Nature*. Springer US, (Ii). doi: 10.1038/s41586-018-0212-1.
- 1021 Masson-Delmotte, V. *et al.* (2011) 'A comparison of the present and last interglacial periods in six
1022 Antarctic ice cores', *Climate of the Past*, 7(2), pp. 397–423. doi: 10.5194/cp-7-397-2011.
- 1023 Matsuda, H. (1978) 'Early diagenesis of fatty acids in lacustrine sediments-III. Changes in fatty acid
1024 composition in the sediments from a brackish water lake', *Geochimica et Cosmochimica Acta*, 42, pp.
1025 1027–1034.
- 1026 Mayer, L. M. (1993) 'Organic Matter at the Sediment-Water Interface', in *Organic Geochemistry:
1027 principles and applications*, pp. 171–184. doi: 10.1007/978-1-4615-2890-6_7.

- 1028 McCartney, M. S. and Donohue, K. A. (2007) 'A deep cyclonic gyre in the Australian-Antarctic Basin',
1029 *Progress in Oceanography*, 75(4), pp. 675–750. doi: 10.1016/j.pocean.2007.02.008.
- 1030 McCave, I. N. and Hall, I. R. (2006) 'Size sorting in marine muds: Processes, pitfalls, and prospects for
1031 paleoflow-speed proxies', *Geochemistry, Geophysics, Geosystems*, 7(10). doi: 10.1029/2006GC001284.
- 1032 McCave, I. N., Manighetti, B. and Robinson, S. G. (1995) 'Sortable silt and fine sediment
1033 size/composition slicing: Parameters for palaeocurrent speed and palaeoceanography',
1034 *Paleoceanography*, 10(3), pp. 593–610. doi: 10.1029/94PA03039.
- 1035 McKay, R. *et al.* (2016) 'Antarctic marine ice-sheet retreat in the Ross Sea during the early Holocene',
1036 *Geology*, 44(1), pp. 7–10. doi: 10.1130/G37315.1.
- 1037 Meyers, P. A. and Ishiwatari, R. (1993) 'Lacustrine organic geochemistry-an overview of indicators of
1038 organic matter sources and diagenesis in lake sediments', *Organic Geochemistry*, 20(7), pp. 867–900.
1039 doi: 10.1016/0146-6380(93)90100-P.
- 1040 Mezgec, K. *et al.* (2017) 'Holocene sea ice variability driven by wind and polynya efficiency in the Ross
1041 Sea', *Nature Communications*. Springer US, 8(1). doi: 10.1038/s41467-017-01455-x.
- 1042 Nielsen, S. H. H. *et al.* (2007) 'Origin and significance of ice-rafted detritus in the Atlantic sector of the
1043 Southern Ocean', *Geochemistry, Geophysics, Geosystems*, 8(12), p. n/a-n/a. doi:
1044 10.1029/2007GC001618.
- 1045 Pagani, M. *et al.* (2006) 'Arctic hydrology during global warming at the Palaeocene/Eocene thermal
1046 maximum', *Nature*, 442(7103), pp. 671–675. doi: 10.1038/nature05043.
- 1047 Paolo, F. S., Fricker, H. A. and Padman, L. (2015) 'Volume loss from Antarctic ice shelves is
1048 accelerating', *Science*, 348(6232), pp. 327–331. doi: 10.1126/science.aaa0940.
- 1049 Peña-Molino, B., McCartney, M. S. and Rintoul, S. R. (2016) 'Direct observations of the Antarctic
1050 Slope Current transport at 113°E', *Journal of Geophysical Research: Oceans*. doi:
1051 10.1002/2015JC011594.
- 1052 Peters, K. E. and Moldowan, J. M. (1993) 'The biomarker guide: interpreting molecular fossils in
1053 petroleum and ancient sediments', *The biomarker guide: interpreting molecular fossils in petroleum and
1054 ancient sediments*. doi: 10.5860/choice.30-2690.
- 1055 Pollard, D. and Deconto, R. M. (2016) 'Contribution of Antarctica to past and future sea-level rise',
1056 *Nature*, 531(7596), pp. 591–597. doi: 10.1038/nature17145.
- 1057 Potter, J. R. and Paren, J. G. (1985) 'Interaction between ice shelf and ocean in George VI Sound,
1058 Antarctica', in *Oceanology of the Antarctic Continental Shelf* (ed S. S. Jacobs), pp. 35–58. doi:
1059 10.1029/AR043p0035.
- 1060 Rhodes, R. H. *et al.* (2012) 'Little Ice Age climate and oceanic conditions of the Ross Sea, Antarctica
1061 from a coastal ice core record', *Climate of the Past*, pp. 1223–1238. doi: 10.5194/cp-8-1223-2012.

- 1062 Riaux-Gobin, C. *et al.* (2011) 'Spring phytoplankton onset after the ice break-up and sea-ice signature
1063 (Adélie Land, East Antarctica)', *Polar Research*, 30(SUPPL.1). doi: 10.3402/polar.v30i0.5910.
1064
- 1065 Riaux-Gobin, C. *et al.* (2013) 'Environmental conditions, particle flux and sympagic microalgal
1066 succession in spring before the sea-ice break-up in Adélie Land, East Antarctica', *Polar Research*, 32,
1067 pp. 0–25. doi: 10.3402/polar.v32i0.19675.
- 1068 Rignot, E. *et al.* (2013) 'Ice Shelf Melting Around Antarctica', *Science*, 1(June), pp. 1–15. doi:
1069 10.1126/science.1235798.
- 1070 Riis, V. and Babel, W. (1999) 'Removal of sulfur interfering in the analysis of organochlorines by GC-
1071 ECD', *Analyst*, 124(12), pp. 1771–1773. doi: 10.1039/a907504f.
- 1072 Robinson, N. J. *et al.* (2014) 'Evolution of a supercooled Ice Shelf Water plume with an actively
1073 growing subice platelet matrix', *Journal of Geophysical Research : Oceans*, pp. 3425–3446. doi:
1074 10.1002/2013JC009399.Received.
- 1075 Sachse, D. *et al.* (2012) 'Molecular Paleohydrology: Interpreting the Hydrogen-Isotopic Composition of
1076 Lipid Biomarkers from Photosynthesizing Organisms', *Annual Review of Earth and Planetary Sciences*,
1077 40(1), pp. 221–249. doi: 10.1146/annurev-earth-042711-105535.
- 1078 Schmidt, G. A., Bigg, G. R. and Rohling, E. J. (1999) *Global Seawater Oxygen-18 Database - v1.22*.
1079 Available at: <https://data.giss.nasa.gov/o18data/>.
- 1080 Schoemann, V. *et al.* (2005) 'Phaeocystis blooms in the global ocean and their controlling mechanisms:
1081 A review', *Journal of Sea Research*, pp. 43–66. doi: 10.1016/j.seares.2004.01.008.
- 1082 Schouten, S. *et al.* (2006) 'The effect of temperature, salinity and growth rate on the stable hydrogen
1083 isotopic composition of long chain alkenones produced by *Emiliania huxleyi* and *Gephyrocapsa*
1084 *oceanica*', *Biogeosciences*, 3(1), pp. 113–119. doi: 10.5194/bg-3-113-2006.
- 1085 Sessions, A. L. *et al.* (1999) 'Fractionation of hydrogen isotopes in lipid biosynthesis, Org', *Organic*
1086 *Geochemistry*, 30, pp. 1193–1200. doi: 10.1016/S0146-6380(99)00094-7.
- 1087 Sessions, A. L. *et al.* (2004) 'Isotopic exchange of carbon-bound hydrogen over geologic timescales',
1088 *Geochimica et Cosmochimica Acta*, 68(7), pp. 1545–1559. doi: 10.1016/j.gca.2003.06.004.
- 1089 Shackleton, N. J. and Kennett, J. P. (1975) 'Paleotemperature history of the Cenozoic and the initiation
1090 of Antarctic glaciation; Oxygen and carbon isotope analyses in DSDP sites 277, 279 and 281', *Initial*
1091 *Reports of the Deep Sea Drilling Project*, 29, pp. 743–755. doi: 10.2973/dsdp.proc.37.1977.
- 1092 Smethie, W. M. and Jacobs, S. S. (2005) 'Circulation and melting under the Ross Ice Shelf: Estimates
1093 from evolving CFC, salinity and temperature fields in the Ross Sea', *Deep-Sea Research Part I:*
1094 *Oceanographic Research Papers*, 52(6), pp. 959–978. doi: 10.1016/j.dsr.2004.11.016.
- 1095 Smik, L., Belt, S.T., Lieser, J.L., *et al.* (2016) Distributions of highly branched isoprenoid alkenes and
1096 other algal lipids in surface waters from East Antarctica: Further insights for biomarker-based paleo sea-
1097 ice reconstruction. *Organic Geochemistry*, 95: 71–80. doi:10.1016/j.orggeochem.2016.02.011.

- 1098 Smith Jr., W. O. *et al.* (2012) ‘the Ross Sea in a Sea of Change’, *Oceanography*, 25(3, SI), pp. 90–103.
- 1099 Solomina, O. N. *et al.* (2015) ‘Holocene glacier fluctuations’, *Quaternary Science Reviews*, pp. 9–34.
1100 doi: 10.1016/j.quascirev.2014.11.018.
- 1101 Spector, P. *et al.* (2017) ‘Rapid early-Holocene deglaciation in the Ross Sea, Antarctica’, *Geophysical*
1102 *Research Letters*, 44(15), pp. 7817–7825. doi: 10.1002/2017GL074216.
- 1103 Steig, E. J. *et al.* (1998) ‘Changes in climate, ocean and ice sheet conditions in the Ross Embayment at 6
1104 ka’, *Annals of Glaciology*, 27, pp. 305–310. doi: 10.3198/1998AoG27-1-305-310.
- 1105 Strickland, J. D. and Parsons, T. R. (1970) ‘J. D. H. Strickland and T. R. Parsons: A Practical Handbook
1106 of Seawater Analysis. Ottawa: Fisheries Research Board of Canada, Bulletin 167, 1968. 293 pp. \$ 7.50’,
1107 in *Internationale Revue der gesamten Hydrobiologie und Hydrographie*, pp. 167–167. doi:
1108 10.1002/iroh.19700550118.
- 1109 Tang, K. W. *et al.* (2008) ‘Colony size of *Phaeocystis antarctica* (Prymnesiophyceae) as influenced by
1110 zooplankton grazers’, *Journal of Phycology*, 44(6), pp. 1372–1378. doi: 10.1111/j.1529-
1111 8817.2008.00595.x.
- 1112 Todd, C., Stone, J., Conway, H., *et al.* (2010) Late Quaternary evolution of Reedy Glacier, Antarctica.
1113 *Quaternary Science Reviews*, 29 (11–12): 1328–1341. doi:10.1016/j.quascirev.2010.02.001.
- 1114 Turner, J. *et al.* (2016) ‘Antarctic sea ice increase consistent with intrinsic variability of the Amundsen
1115 sea low’, *Climate Dynamics*. Springer Berlin Heidelberg, 46(7–8), pp. 2391–2402. doi: 10.1007/s00382-
1116 015-2708-9.
- 1117 Wong, W. W. and Sackett, W. M. (1978) ‘Fractionation of stable carbon isotopes by marine
1118 phytoplankton’, *Geochimica et Cosmochimica Acta*, 42(12), pp. 1809–1815. doi: 10.1016/0016-
1119 7037(78)90236-3.
- 1120 Zhang, J. and Hibler, W. D. (1997) ‘On an efficient numerical method for modeling sea ice dynamics’,
1121 *Journal of Geophysical Research*, 102(C4), p. 8691. doi: 10.1029/96JC03744.
- 1122 Zhang, Z., Sachs, J. P. and Marchetti, A. (2009) ‘Hydrogen isotope fractionation in freshwater and
1123 marine algae: II. Temperature and nitrogen limited growth rate effects’, *Organic Geochemistry*, 40(3),
1124 pp. 428–439. doi: 10.1016/j.orggeochem.2008.11.002.
- 1125
1126

1127 **Acknowledgements:** Samples and data were provided by the International
1128 Ocean Discovery Program (IODP). The Natural Environment Research Council funded K.E.A (CENTA
1129 PhD; NE/L002493/1) and J.B. (Standard Grant Ne/I00646X/1). J.B. and O.S. were funded by Japanese
1130 Society for the Promotion of Science (JSPS/FF2/60 No. L-11523). R.M. and N.B were funded by the
1131 NZ Marsden Fund (18-VUW-089 and 15-VUW-131). A.C. was funded by the NSF (PLR-1443347) and
1132 the U.S. Dept. of Energy (DE-SC0016105). A.C. performed model integrations at the National Research
1133 Scientific Computing Center and at XSEDE, an NSF funded computer center (grant ACI-1548562).
1134 C.R. was funded by a L’Oréal-UNESCO New Zealand For Women in Science Fellowship, University of

1135 Otago Research Grant, and the IODP U.S. Science Support Program. We thank S. Schouten, V.
1136 Willmott, F. Sangiorgi, J. Toney and J. Pike for discussions and V. Willmott, H. Moossen, A. Hallander,
1137 R. Jamieson and C. Gallagher for technical support.

1138
1139 **Author contributions:** K.E.A., J.B and R.M. wrote the paper. J.B. and O.S. carried out the fatty acid
1140 isotope analysis, A.A. and R.M. conducted the grain size analyses, J.E. and G.M. generated the HBI
1141 data, F.J.J.E measured X-ray fluorescence scanning and electron microscopy, and C.R conducted the
1142 opal measurements. R.D., R.M., X.C. and G.M. developed the age model. A.C ran the model
1143 simulations. D.P.L and E.G analysed the Trace-21k experiment data. R.D. was lead proponent on the
1144 U1357 drilling proposal. All authors contributed to the interpretations of data and finalization of the
1145 manuscript.

1146
1147 **Competing interests:** The authors have no competing interests.

1148
1149 **Data availability:** There is no restriction on data availability. Upon manuscript acceptance, all
1150 previously unpublished data will be added to the Supplementary Materials and made freely available at
1151 the NOAA NCDC data-base: <https://www.ncdc.noaa.gov/data-access/paleoclimatology-data/datasets>.

1152
1153
1154
1155

SUPPLEMENTARY MATERIALS

S1. Age model

We developed an age model for core U1357B based on 87 ¹⁴C analyses on bulk organic carbon (Fig. S1). In the standard IODP CSF-A depth scale, recovery often exceeds 100% and to correct for this, the standard IODP procedure is to apply a linear compression algorithm which is based on the assumption that expansion is uniform in the core. However, in U1357B, expansion due to biogenic gas was particularly high and resulted in discrete sections of core being pushed apart creating voids in the depth scale that did not represent real gaps in the stratigraphy. To account for this, the voids are numerically removed and depth scale adjusted prior to linear compression being applied (if recovery still exceeds 100%).

The model was calibrated with a reservoir age correction of 1200±100 years and depth to age conversions achieved by using BACON. This is a Bayesian iteration scheme that invokes memory from dates above any given horizon, and produces a weighted mean and median age-depth curve

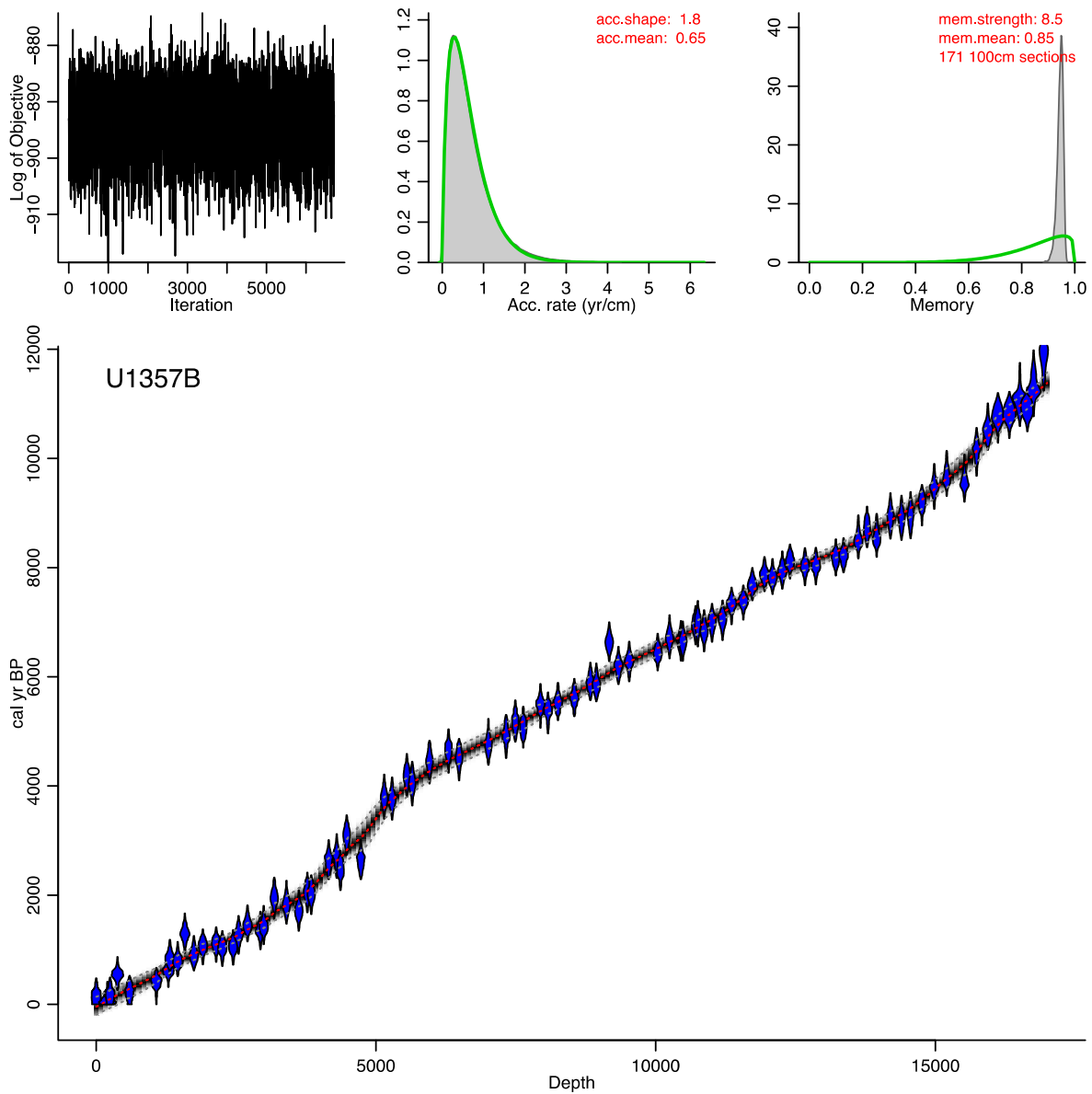


Figure S1. Age-depth plot of U1357B, using the default outputs from the BACON software. Upper panels show (from left to right): a stationary distribution of the Markov Chain Monte Carlo iterations; prior (green curve) and posterior (grey curve) distribution for the accumulation rate; prior (green curve) and posterior (grey curve) distribution for memory. Bottom panel shows the calibrated ^{14}C dates (blue) and age depth model with 95% confidence intervals.

(Blaauw and Christeny, 2011). The top depth of 3 m is consistent with the reservoir age in the Southern Ocean (Hall et al., 2010). Bulk organic carbon ages in the Antarctic are commonly compromised by reworking of older carbon in the sediment column (Andrews et al., 1999), which is compounded by extreme sediment starvation of post-LGM sequences in the Antarctic. However, due

to extremely high input of autochthonous carbon associated with the Adélie Drift deposit, which is a predominately seasonally deposited

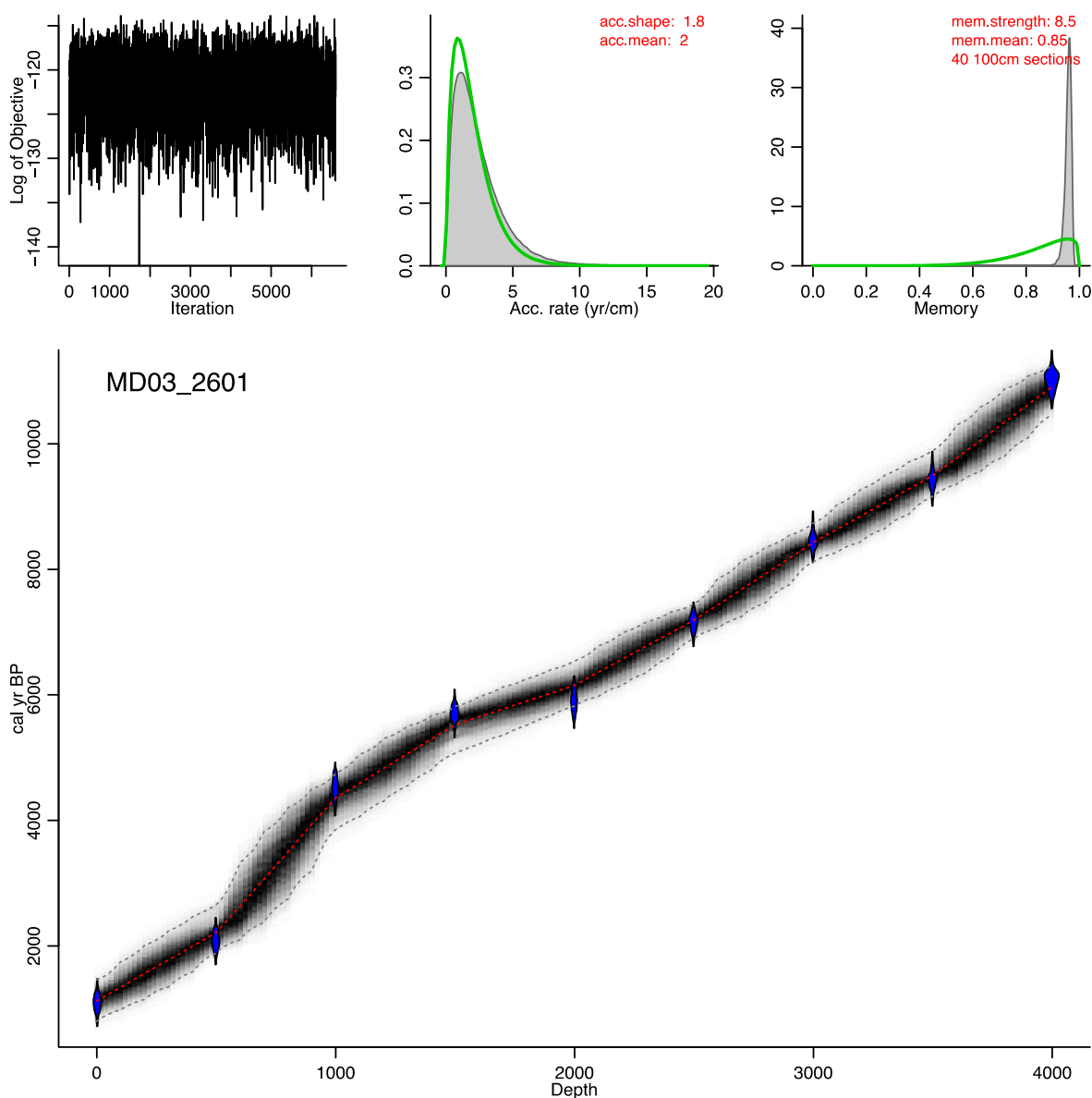


Figure S2. Age-depth plot of MD03-2601, using the default outputs from the BACON software. Upper panels show (from left to right): a stationary distribution of the Markov Chain Monte Carlo iterations; prior (green curve) and posterior (grey curve) distribution for the accumulation rate; prior (green curve) and posterior (grey curve) distribution for memory. Bottom panel shows the calibrated ^{14}C dates (blue) and age depth model with 95% confidence intervals.

diatom bloom, this reworking is expected to be minimal at the U1357 site, and is only a potential issue at the base of the core (Unit II), due to increased proximity to glacial influences from the Adélie Land coast during the deglaciation (e.g. > 11.4 ka). This is supported by the radiocarbon ages,

maintaining a strong stratigraphic order (within error), relatively consistent sedimentation rates throughout the deposited interval, and core top ages that are consistent with the expected reservoir age.

We also recalibrated the age-model for MD03-2601 applying the BACON methodology using the ^{14}C dates presented in (Crosta et al., 2008) (Fig. S2). This age model differs from that of (Denis et al., 2009a), who discarded two ^{14}C ages bracketing the mid-Holocene (4.4 and 5.6 cal ka BP), on the basis of an inferred meteorite impact at ca. 15 m and correlated this to an event at 4 ka BP. We note that this impact correlation does not provide a unique absolute age constraint, with our revised age model instead indicating an age of 5.4 cal ka BP for this impact event. Critically, comparison between the age model for U1357B and the revised age model for MD03-2601 now indicates a strong similarity regarding changes in the sedimentation rates at ca. 4.5 ka and ca. 2 ka BP, indicating that both sites are influenced by similar depositional processes.

S2. Further details on interpretation of proxy data

S2.1 Ba/Ti ratio excess as a primary productivity proxy

Ba-based proxies (e.g., Ba/Ti or equivalent Ba/Al) in the Wilkes Land margin sediments have been commonly related to marine productivity (Presti et al., 2011), although studies in other pelagic environments indicate that they can also be sensitive to bottom current intensity (Bahr et al., 2014), meltwater (Plewa et al., 2006), and other processes (Griffith and Paytan, 2012). FESEM analysis and images at Site U1357 indicate the presence of biogenic barite (Fig. S3a), recognized by the elliptical morphologies and sizes between 1 to 3 μm (Paytan et al., 2002). Titanium is found associated with small heavy minerals (ilmenite) with angular and low sphericity shapes.

Along the entire record, Ba/Ti ratios show persistent periodic fluctuations with values between 0.1 and 2.7. Nevertheless, a marked enrichment can be observed at 4.5 ka reaching Ba/Ti ratio values

over 36.1 (Fig. 2). Pore water analysis indicates that the carbon dioxide (methanic) reduction zone (CRZ) is reached just few cm near sea floor and the upper 20 m already contain sulfate-free interstitial waters (Escutia et al., 2011). Observed geochemical conditions indicate that some Barite dissolution could be expected, but there is no diagenetic barite that could justify the obtained enrichment. In addition, at the enriched interval we did not observe any lithological change or enrichment in other elements (e.g., Si). The influence of aeolian dust or fluvial input on Ba input can also be discarded in the glaciated Wilkes Land margin. In the same way, Ba concentration in sea-ice is considered null because on an annual cycle, sea ice does not constitute a net source or sink of these species to the underlying seawater (Thomas, 2011).

Furthermore, FESEM imaging detected biogenic barite during intervals where the Ba/Ti excess occurs (Fig. S3) pointing to an increase in productivity. This may be driven by water column stratification

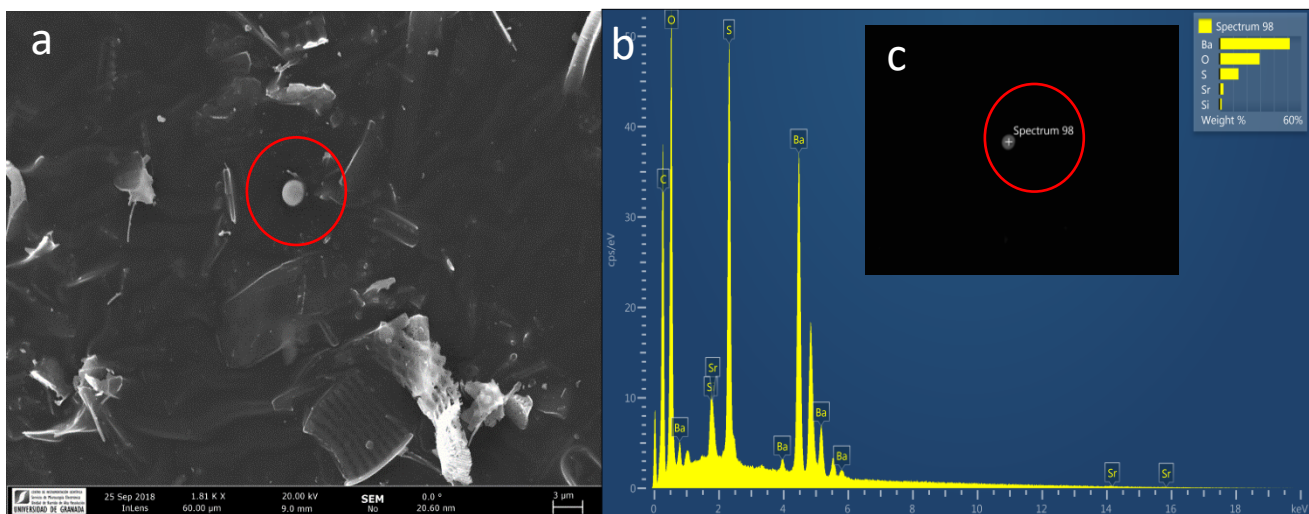


Figure S3. Authigenic marine barite (red circle, size > 300nm) observed in Ba/Ti enriched interval (sample U1357B-8H-2A 141-143; age: 4,430 cal yr) a) SEM image obtained with secondary electrons with Inlens detector at 20 kV b) SEM-EDX spectrum (analyzed spot marked with a white cross in image c)) showing barite composition (BaSO_4) c) Same barite shown in a backscattered electron (BSE) mode by AsB detector at 20 kV.

or greater nutrient availability. This interpretation is coherent with other paleoproductivity reconstructions in this area, in particular peaks in ^{230}Th -normalized fluxes of biogenic silica (BSi) and organic carbon content recorded in nearby core MD03-2601 (Denis et al., 2009b) (when using the recalibrated age-model – see S2).

S2.2 Grain size

Grainsize analysis was conducted on paired samples with lipid biomarker samples in Unit I. Unit I represents the onset of the modern deposition at Site U1357, and the underlying stratigraphy is discussed in the main text. Between ca. 11.4 and 8 ka, U1357B has a relatively high terrigenous component (i.e. high Natural Gamma Radiation (NGR) content and low BSi%; Fig 4). The grain size distribution contains coarse tails of fine (125-250 μm) to medium sands (250-500 μm), but only one sample contains coarse sands (>500 μm) that may represent ice-berg rafted debris (IBRD). However, terrigenous content and IBRD is more common in the underlying Unit II, which is interpreted to represent a true “calving bay environment” (Escutia et al., 2011). Shipboard description of the core faces found the presence of small isolated faceted and striated pebbles (lonestones) in Unit II (Escutia et al., 2011), which is supportive of an iceberg component to sediment supply, but these are largely absent in Unit I. The fine grained sands and muds have a distribution with similar modes to overlying intervals, albeit with an increase in the size of the coarse silt and very fine sand modes. The subtle increased sorting up core between ca. 11.4 and ca.8 ka (from very poorly to poorly sorted, Fig. 4) is consistent with an increasingly more distal setting, with less potential for a glacial grounding line sediment supply (Powell and Domack, 1995; McKay et al., 2009). This interval is interpreted to reflect the final post-LGM retreat of local EAIS outlet glacier grounding lines from a proximal (less sorted, more IBRD) to more distal setting (better sorted, less IBRD) from the site, although we note a much larger shift occurs at the Unit I/II boundary at 170.25 mbsf (ca.11.4 ka) (Escutia et al., 2011) and dominant sediment supply from local outlet glaciers probably ceased at this earlier time. It is likely this distal setting was close to the modern day grounding line, as the Dumont d’Urville Trough is overdeepened between Site U1357 and the modern day grounding line, and this bathymetry configuration is inherently unstable for marine-based ice sheets (Thomas and Bentley, 1978; Bentley et al., 2014).

Today, Adélie Land glaciers are inferred to have relatively clean basal layers due to the solid bedrock (Kleinschmidt and Talarico, 2000), and distal polar glacimarine settings are usually sediment starved and provide very low inputs of terrigenous sediments (Powell and Domack, 1995; McKay et al., 2009).

There are also no large proglacial fans evident at the mouths of these glaciers (Beaman et al., 2011) and consequently, direct sediment discharge from the Mertz and Ninnis Glaciers is unlikely to be of significant quantity to sustain dense overflows delivering sediment over the Adélie Bank and into the Dumont d'Urville Trough. Therefore, the release of terrigenous material through glacial melting is low (to absent) when glacier activity is steady and distal from the site, but is anticipated to increase with increased proximity to the glacier front or with enhanced dynamic ice discharge (which may occur either during a retreat or advance), which would be associated with an increase in IBRD from local outlet glaciers. We note evidence for proglacial fan deposition and IBRD is lacking throughout Unit I (post 11.4 ka).

Between 9 and 4.5 ka, mass accumulation rates (MARs) (both biogenic and terrigenous; Fig. S4) are relatively high, albeit with millennial scale variability. However, the mean grain size and sorting of the terrigenous material is relatively stable throughout the entire interval, and as with the rest of Unit I there is an almost complete lack of IBRD. This suggests that sediment input from grounding line processes were also minimal through this time. Based on the drift morphology (Fig S4), and the prevailing easterly flow of the Antarctic Coastal Current, this interval is interpreted to be the result of sediment advection to the site from the east as residual ice retreated from the bathymetric highs in the region. Diatom frustules and sponge spicules are mainly in the 16 to 63 μm range, much of which is maintained in suspension by weak currents (a few cm s^{-1}) (Dunbar et al., 1985). The greater area of open water for primary production during the summer, combined with an open pathway for

advection of biogenic matter from the MGP (Fig. 1) can thus explain the significant rise in linear sedimentation and mass accumulation rates for both biogenic and terrigenous material. Most of the terrigenous material after ~8 ka is proposed to have been primarily eroded off the Adélie Bank by westward flowing currents into the Adélie drift where sediment would have settled out from suspension. Terrigenous sediment younger than 8 ka in this drift is almost entirely finer than 125 μm , while Dunbar et al. (1985) revealed that surface sediments on shallow banks have a grain size distribution that generally exceeds 125 μm . This supports our interpretation that the majority of the terrigenous material in U1357B is winnowed from these banks by bottom currents. The size of the material winnowed implies that maximum current velocities in the region are greater than 18-20 cm s^{-2} , the minimum velocity required to transport fine sand by intermittent suspension and suspension in poorly sorted glacial marine settings (Singer and Anderson, 1984; McCave and Hall, 2006).

The complete lack of medium to coarse sand in the grain size distributions of Unit I (<11.4 ka), and from visual observation of the core face, that may represent IBRD may be the consequence that icebergs calved from large ice shelves and ice tongues, such as the RIS and Mertz Glacier Tongue, are advected into the region via the Antarctic Coastal Current but usually lack basal debris. While the lack of IBRD could in part be explained as the consequence of the widespread development of the RIS in the Holocene (McKay et al., 2016), it could also be due to the Adélie and Mertz Banks (and Mertz Glacier Tongue) acting to shield Site U1357 from large icebergs passing over the site, as icebergs would have become grounded on the bathymetric highs and deflected north (Massom et al., 2001; Beaman et al., 2011). Notably, this lack of IBRD further supports a lack of shifting glacial dynamics and calving of sediment-laden icebergs from the smaller local Astrolabe and Zélée outlet glaciers through this time.

There is a rapid increase in mud content at 4.5 ka coincident with a reduction in both the biogenic and terrigenous MARs, although the terrigenous MAR curve shows higher

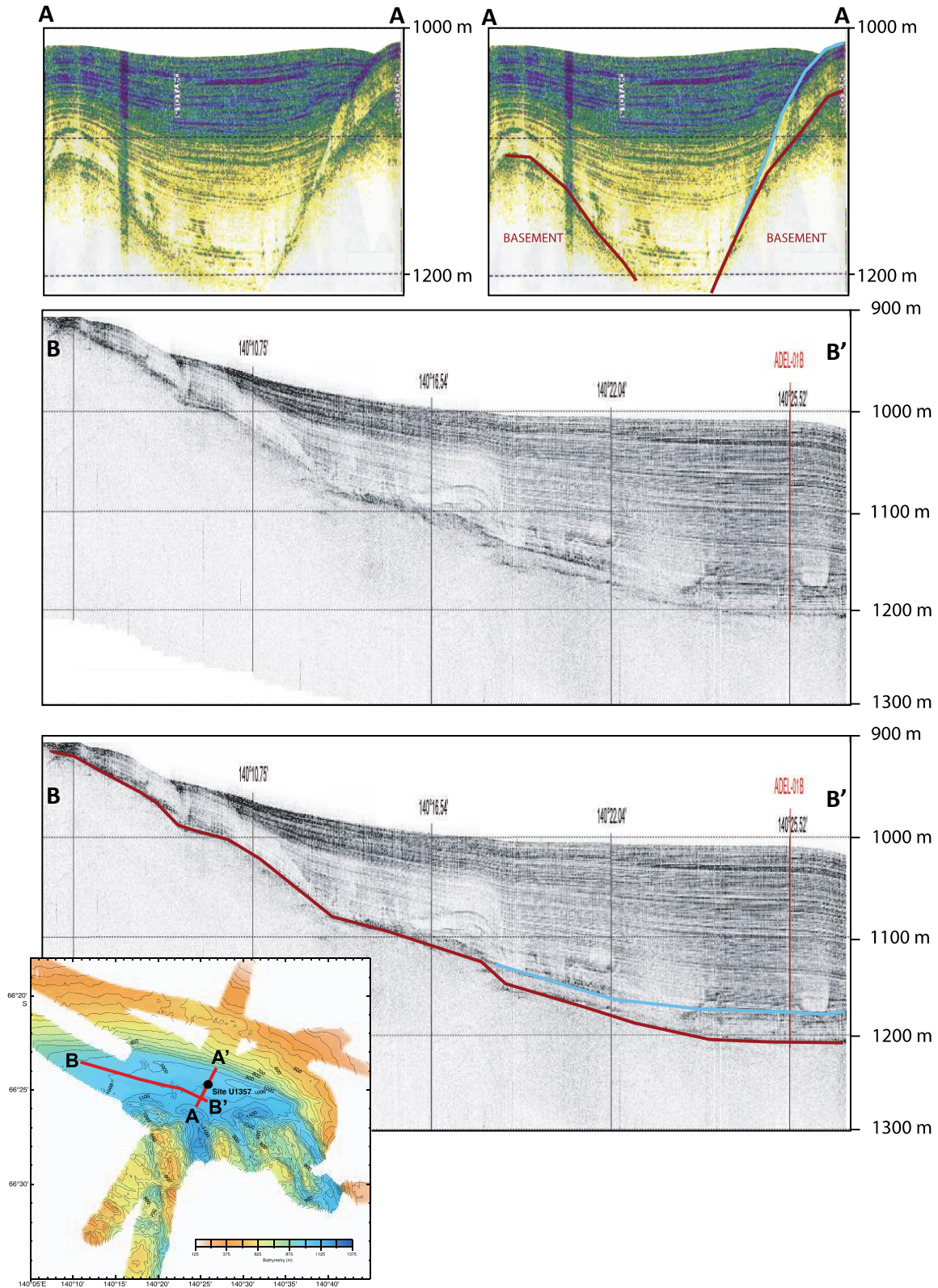


Figure S4 3.5 kHz seismic profile of the Adélie drift. Top: South (A) to north (A') profile, showing early Holocene (inferred to be ~11-8.2 ka) strata downlapping on top the basement highs (blue reflector and below). This is overlain by onlapping strata (blue reflector and above). Middle and Bottom: West (B) to East (B') profile, showing that in the depocentre of the basin, the pre-8.2 strata has a different geometry to overlying strata (onlapping onto the northern bank of the Dumont D'Urville Trough), suggesting a supply from the south, while overlying strata form a drift deposit that is thickest on the northern flank of the trough, and infers a drift deposit morphology that is aligned with the flow of easterly Antarctic Coastal Current.

accumulation rates than the biogenic MAR curve (Fig. 4). Hence, less material is being advected to the site, and the maximum current strength acting to winnow and advect material from the Adélie Bank into the Dumont d'Urville Trough is reduced. A reduction in maximum current strength could potentially be explained by more extensive sea ice over the site, which would act to reduce wind stress on the ocean surface and thus the maximum strength of the easterly flow, despite enhanced zonal easterly winds that are predicted with a cooler Antarctic climate (Shin et al., 2003; DeConto et al., 2007).

A final consideration is that aeolian contribution of terrigenous material is known to be of importance in Antarctic coastal areas affected by katabatic winds (Atkins and Dunbar, 2009; Chewings et al., 2014). However, windblown sediment is usually well-sorted, and combined with the lack of exposed sediment in Wilkes Land, and the distance of the core site from the coast, input of aeolian sediment into the ocean from melting sea ice is likely to be a relatively minor component of the sediment population relative to the suspended sediment load derived from the local banks and pelagic processes.

S2.3. Highly-branched isoprenoids (HBI)

Several recent studies have highlighted the strong potential of the HBI biomarkers along the Antarctic coast as a robust proxy of sea ice extent. Indeed, it has been shown that the di-unsaturated HBI lipid (i.e. diene II or C_{25:2} alkene) is only synthesized in the modern Antarctic waters by sea ice-associated diatoms (Belt et al., 2016; Massé et al., 2011; Smik et al., 2016). The tri-unsaturated HBI lipid (i.e. triene III or C_{25:3}) is in contrast strictly produced by open water diatom species, which have been found to be in highest abundance in the marginal ice zone (Smik et al., 2016). Thus, the calculated diene/triene ratio is a reliable tracer to qualitatively estimate the sea ice extent (sea ice vs open water conditions). As previously applied in various Antarctic coastal sediments during different period of time (Etourneau et al., 2013; Collins et al., 2012; Barbara et al., 2010), the diene/triene

ratio was successfully used to reconstruct the past sea ice history around Antarctica. In particular, it has been shown that the HBIs were not significantly affected by (i) changes in sources (glacial ice vs sea ice), as the diatoms producing the HBIs strictly grow in relation with sea ice (under or at the edge) (ii) bacterial degradation (Robson and Rowland, 1988) or (iii) rapid sulfurization under anoxic conditions (Sinninghe Damsté et al., 2007). Absolute concentrations of the HBI diene and triene compounds are shown in Fig. S5.

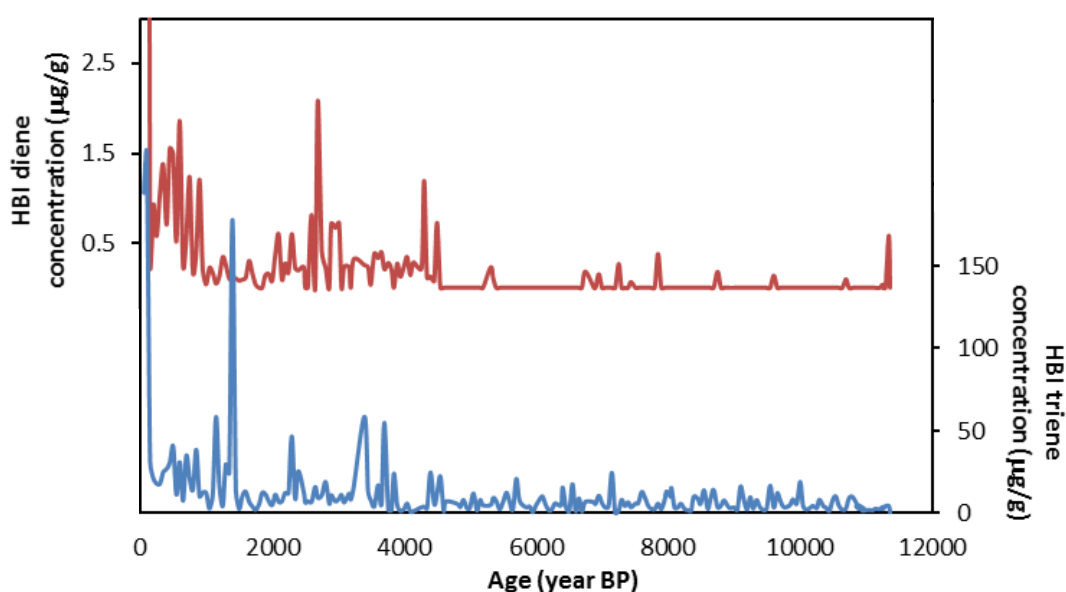


Figure S5 Absolute concentrations of highly branched isoprenoids (HBIs) measured in U1357B.

S3. Data-Model mismatch

Comparison of sea ice data from the Adélie region (presented in this study), with model output for sea ice thickness and extent from TraCE-21k simulations, indicates a clear mismatch between the observational data and model output over the Holocene (Fig. S6). The rapid mid-Holocene increase in sea ice, recorded at Site U1357 and other sites in the Antarctic coastal zone (Fig. S6c, d), is not seen in the model simulations, which instead indicate a sharp decline in sea ice extent and thickness around the Antarctic and in the Adélie region after ca. 5 ka (Fig. S6a, b). The Community Climate

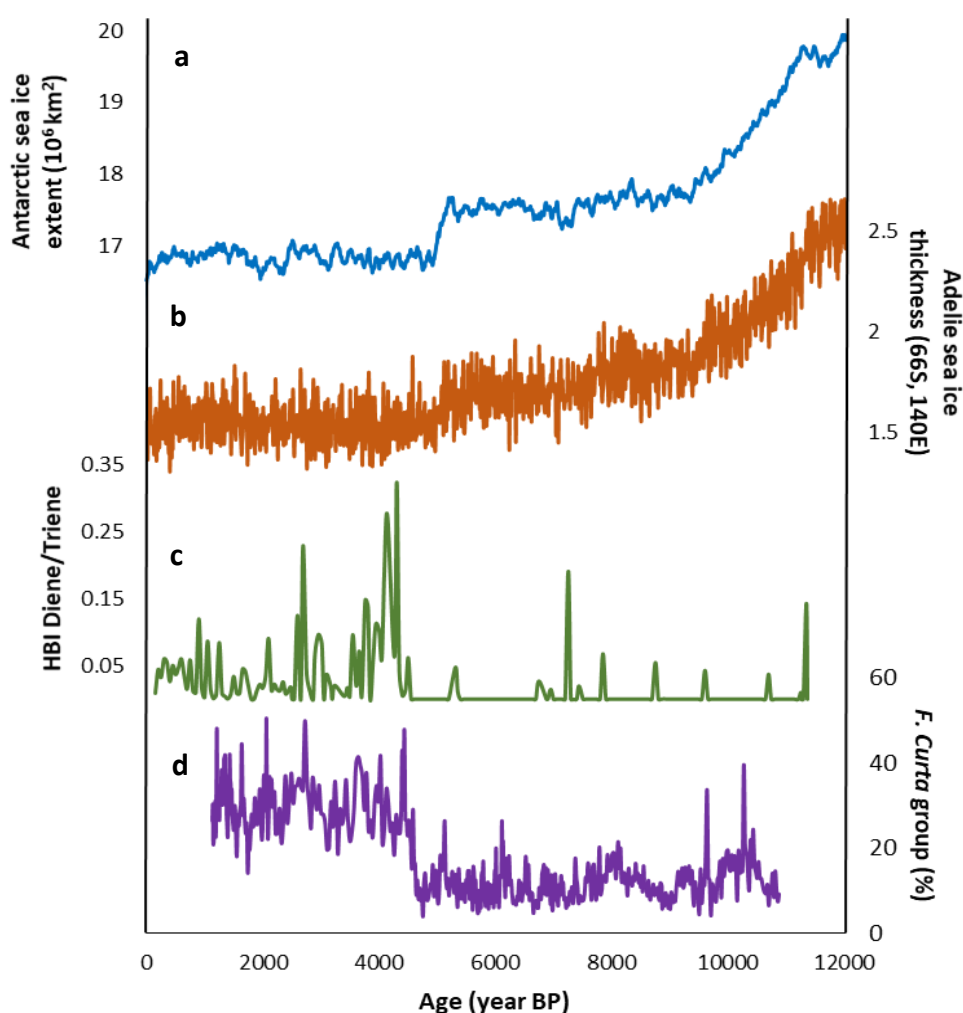


Figure S6 Comparison of sea ice data from the Adélie region with TraCE-21k simulations a) Antarctic sea ice extent (10^6 km^2) from TraCE-21k b) Adélie sea ice thickness (66°S , 140°E) from TraCE-21k c) Ratio of the di-unsaturated HBI (C25:2; Diene) and the tri-unsaturated HBI isomer (C25:3; Triene) at Site U1357 d) *Fragilariopsis curta* group relative abundances from MD03-2601.

System Model (CCSM3) used in the simulations lacks a dynamic ice sheet, instead using a constant

prescribed meltwater flux of 1.12 m ka^{-1} from the Antarctic which finishes at 5 ka, which can likely explain the simulated sea-ice decline at ca. 5 ka. Furthermore, it does not incorporate ice-ocean coupling or ice shelf cavities. We have shown that these processes have an important role on sea ice production and thus are required within models to capture the coupled response between ice sheets and the ocean. We note that some models, such as LOVECLIM (Renssen et al., 2010), do simulate a gradual sea-ice increase and cooling trend in the late Holocene, however the timing (gradual) and magnitude (subtle) of sea-ice trends do not match the abrupt and large changes seen in the proxy data.

Supplementary material references

Andrews, J.T., Domack, E.W., Cunningham, W.L., et al. (1999) Problems and possible solutions concerning radiocarbon dating of surface marine sediments, Ross Sea, Antarctica. *Quaternary Research*, 52 (2): 206–216. doi:10.1006/qres.1999.2047.

Atkins, C.B. and Dunbar, G.B. (2009) Aeolian sediment flux from sea ice into Southern McMurdo Sound, Antarctica. *Global and Planetary Change*, 69 (3): 133–141. doi:10.1016/j.gloplacha.2009.04.006.

Bahr, A., Jiménez-Espejo, F.J., Kolasinac, N., et al. (2014) Deciphering bottom current velocity and paleoclimate signals from contourite deposits in the Gulf of Cádiz during the last 140 kyr: An inorganic geochemical approach. *Geochemistry, Geophysics, Geosystems*, 15 (8): 3145–3160. doi:10.1002/2014GC005356.

Barbara, L., Crosta, X., Massé, G., et al. (2010) Deglacial environments in eastern Prydz Bay, East Antarctica. *Quaternary Science Reviews*, 29 (19–20): 2731–2740. doi:10.1016/j.quascirev.2010.06.027.

Beaman, R.J., O'Brien, P.E., Post, A.L., et al. (2011) A new high-resolution bathymetry model for the Terre Adélie and George V continental margin, East Antarctica. *Antarctic Science*, 23 (1): 95–103. doi:10.1017/S095410201000074X.

Belt, S.T., Smik, L., Brown, T.A., et al. (2016) Source identification and distribution reveals the potential of the geochemical Antarctic sea ice proxy IPSO25. *Nature Communications*, 7: 12655. doi:10.1038/ncomms12655.

Bentley, M.J., Ocofaigh, C., Anderson, J.B., et al. (2014) A community-based geological reconstruction of Antarctic Ice Sheet deglaciation since the Last Glacial Maximum. *Quaternary Science Reviews*, 100: 1–9. doi:10.1016/j.quascirev.2014.06.025.

Blaauw, M. and Christeny, J.A. (2011) Flexible paleoclimate age-depth models using an autoregressive gamma process. *Bayesian Analysis*, 6 (3): 457–474. doi:10.1214/11-BA618.

- Chewings, J.M., Atkins, C.B., Dunbar, G.B., et al. (2014) Aeolian sediment transport and deposition in a modern high-latitude glacial marine environment. *Sedimentology*, 61 (6): 1535–1557. doi:10.1111/sed.12108.
- Collins, L.G., Pike, J., Allen, C.S., et al. (2012) High-resolution reconstruction of southwest Atlantic sea-ice and its role in the carbon cycle during marine isotope stages 3 and 2. *Paleoceanography*, 27 (3). doi:10.1029/2011PA002264.
- Crosta, X., Denis, D. and Ther, O. (2008) Sea ice seasonality during the Holocene, Adelie Land, East Antarctica. *Marine Micropaleontology*, 66 (3–4): 222–232. doi:10.1016/j.marmicro.2007.10.001.
- DeConto, R., Pollard, D. and Harwood, D. (2007) Sea ice feedback and Cenozoic evolution of Antarctic climate and ice sheets. *Paleoceanography*, 22 (3). doi:10.1029/2006PA001350.
- Denis, D., Crosta, X., Schmidt, S., et al. (2009a) Holocene glacier and deep water dynamics, Adélie Land region, East Antarctica. *Quaternary Science Reviews*. doi:10.1016/j.quascirev.2008.12.024.
- Denis, D., Crosta, X., Schmidt, S., et al. (2009b) Holocene productivity changes off Adélie land (East Antarctica). *Paleoceanography*, 24 (3): 1–12. doi:10.1029/2008PA001689.
- Dunbar, R.B., Anderson, J.B., Domack, E.W., et al. (1985) “Oceanographic influences on sedimentation along the Antarctic continental shelf.” In *Oceanology of the Antarctic Continental Shelf* (eds S. Jacobs). pp. 291–312. doi:10.1029/AR043p0291.
- Escutia, C., Brinkhuis, H. and Klaus, A. (2011) Site summary. *Proc. IODP* /, 318: 1–74. doi:10.2204/iodp.proc.318.105.2011.
- Etourneau, J., Collins, L.G., Willmott, V., et al. (2013) Holocene climate variations in the western Antarctic Peninsula: Evidence for sea ice extent predominantly controlled by changes in insolation and ENSO variability. *Climate of the Past*, 9 (4): 1431–1446. doi:10.5194/cp-9-1431-2013.
- Folk, R.L. and Ward, W.C. (1957) Brazos River bar [Texas]; a study in the significance of grain size parameters. *Journal of Sedimentary Research*, 27 (1): 3–26. doi:10.1306/74D70646-2B21-11D7-8648000102C1865D.
- Griffith, E.M. and Paytan, A. (2012) Barite in the ocean - occurrence, geochemistry and palaeoceanographic applications. *Sedimentology*, 59 (6): 1817–1835. doi:10.1111/j.1365-3091.2012.01327.x.
- Hall, B.L., Henderson, G.M., Baroni, C., et al. (2010) Constant Holocene Southern-Ocean14C reservoir ages and ice-shelf flow rates. *Earth and Planetary Science Letters*, 296 (1–2): 115–123. doi:10.1016/j.epsl.2010.04.054.
- Kleinschmidt, G. and Talarico, F. (2000) The Mertz shear zone. *Terra Antarctica Reports*, pp. 109–115.
- Massé, G., Belt, S.T., Crosta, X., et al. (2011) Highly branched isoprenoids as proxies for variable sea ice conditions in the Southern Ocean. *Antarctic Science*, 23 (5): 487–498. doi:10.1017/S0954102011000381.
- Massom, R.A., Hill, K.L., Lytle, V.I., et al. (2001) Effects of regional fast-ice and iceberg distributions on the behaviour of the Mertz Glacier polynya, East Antarctica. *Annals of Glaciology*,

33: 391–398. doi:10.3189/172756401781818518.

McCave, I.N. and Hall, I.R. (2006) Size sorting in marine muds: Processes, pitfalls, and prospects for paleoflow-speed proxies. *Geochemistry, Geophysics, Geosystems*, 7 (10). doi:10.1029/2006GC001284.

McKay, R., Browne, G., Carter, L., et al. (2009) The stratigraphic signature of the late Cenozoic Antarctic Ice Sheets in the Ross Embayment. *Bulletin of the Geological Society of America*, 121 (11–12): 1537–1561. doi:10.1130/B26540.1.

McKay, R., Gollledge, N.R., Maas, S., et al. (2016) Antarctic marine ice-sheet retreat in the Ross Sea during the early Holocene. *Geology*, 44 (1): 7–10. doi:10.1130/G37315.1.

Paytan, A., Mearon, S., Cobb, K., et al. (2002) Origin of marine barite deposits: Sr and S isotope characterization. *Geology*, 30 (8): 747–750. doi:10.1130/0091-7613(2002)030<0747:OOMBDS>2.0.CO;2.

Plewa, K., Meggers, H. and Kasten, S. (2006) Barium in sediments off northwest Africa: A tracer for paleoproductivity or meltwater events? *Paleoceanography*, 21 (2): 1–15. doi:10.1029/2005PA001136.

Powell, R. and Domack, E. (1995) “Glaciomarine processes and sediments.” In *Modern Glacial Environments* (Eds J. Menzies). Butterworth-Heinemann, Oxford.

Presti, M., Barbara, L., Denis, D., et al. (2011) Sediment delivery and depositional patterns off Adélie Land (East Antarctica) in relation to late Quaternary climatic cycles. *Marine Geology*, 284 (1–4): 96–113. doi:10.1016/j.margeo.2011.03.012.

Renssen, H., Goosse, H., Crosta, X., et al. (2010) Early holocene laurentide ice sheet deglaciation causes cooling in the high-latitude southern hemisphere through oceanic teleconnection. *Paleoceanography*, 25 (3): 1–15. doi:10.1029/2009PA001854.

Robson, J.N. and Rowland, S.J. (1988) Biodegradation of highly branched isoprenoid hydrocarbons: A possible explanation of sedimentary abundance. *Organic Geochemistry*, 13 (4–6): 691–695. doi:10.1016/0146-6380(88)90090-3.

Shin, S.-I., Liu, Z., Otto-Bliesner, B.L., et al. (2003) Southern Ocean sea-ice control of the glacial North Atlantic thermohaline circulation. *Geophysical Research Letters*, 30 (2). doi:10.1029/2002GL015513.

Singer, J.K. and Anderson, J.B. (1984) Use of total grain-size distributions to define bed erosion and transport for poorly sorted sediment undergoing simulated bioturbation. *Marine Geology*, 57 (1–4): 335–359. doi:10.1016/0025-3227(84)90204-4.

Sinninghe Damsté, J.S., Rijpstra, W.I.C., Coolen, M.J.L., et al. (2007) Rapid sulfurisation of highly branched isoprenoid (HBI) alkenes in sulfidic Holocene sediments from Ellis Fjord, Antarctica. *Organic Geochemistry*, 38 (1): 128–139. doi:10.1016/j.orggeochem.2006.08.003.

Smik, L., Belt, S.T., Lieser, J.L., et al. (2016) Distributions of highly branched isoprenoid alkenes and other algal lipids in surface waters from East Antarctica: Further insights for biomarker-based paleo sea-ice reconstruction. *Organic Geochemistry*, 95: 71–80. doi:10.1016/j.orggeochem.2016.02.011.

Thomas, D.N. (2011) “Biogeochemistry of Sea Ice.” *In Encyclopedia of Snow, Ice and Glaciers* (eds Singh V.P., Singh P., Haritashya U.K.). pp. 98–102. doi:10.1007/978-90-481-2642-2_639.

Thomas, R.H. and Bentley, C.R. (1978) A model for Holocene retreat of the West Antarctic Ice Sheet. *Quaternary Research*, 10 (2): 150–170. doi:10.1016/0033-5894(78)90098-4.